

[Click here to view linked References](#)

## Experimental constraints on the textures and origin of obsidian pyroclasts

James E. Gardner<sup>a,\*</sup>, Fabian B. Wadsworth<sup>b</sup>, Edward W. Llewelin<sup>b</sup>, James M. Watkins<sup>c</sup>,  
and Jason P. Coumans<sup>b</sup>

<sup>a</sup>*Department of Geological Sciences, Jackson School of Geosciences, The University of Texas at  
Austin, Austin, TX, 78712-0254, U.S.A.*

<sup>b</sup>*Department of Earth Sciences, Science Labs, Durham University, Durham, DH1 3LE, U.K.*

<sup>c</sup>*Department of Earth Sciences, University of Oregon, Eugene, OR, 97403-1272, U.S.A.*

\*Corresponding author. Fax: +1 512 471 9425

E-mail address: [gardner@mail.utexas.edu](mailto:gardner@mail.utexas.edu) (J.E. Gardner)

1 **Abstract**

2 Obsidian pyroclasts are commonly preserved in the fall deposits of explosive silicic eruptions.  
3 Recent work has suggested that they form by sintering of ash particles on the conduit walls above  
4 the fragmentation depth, and are subsequently torn out and transported in the gas–particle  
5 dispersion. Although the sintering hypothesis is consistent with the general vesicle textures and  
6 dissolved volatiles in obsidian pyroclasts, previous sintering experiments do not capture all of the  
7 textural complexities observed in the natural pyroclasts. Here, we design experiments in which  
8 unimodal and bimodal distributions of rhyolitic ash are sintered at temperatures and H<sub>2</sub>O  
9 pressures relevant to shallow volcanic conduits, and under variable cooling rates. The  
10 experiments produce dense, welded obsidian that have a range of textures similar to those  
11 observed in natural pyroclasts. We find that using a unimodal distribution of particles produces  
12 obsidian with evenly distributed trapped vesicles, while a bimodal initial particle distribution  
13 produces obsidian with domains of poorly vesicular glass among domains of more vesicle-rich  
14 glass. We also find that slow cooling leads to resorption of trapped vesicles, producing fully dense  
15 obsidian. These broad features match those found in obsidian pyroclasts from the North Mono  
16 (California, USA) rhyolite eruption, providing strong support to the hypothesis that obsidian can  
17 be produced by ash sintering above the fragmentation depth during explosive eruptions.

18

19 Keywords: obsidian; ash; sinter; volatile; explosive eruption

20

21 **Introduction**

22

23 Obsidian pyroclasts – pieces of glassy rhyolite found in tephra deposits – have played a central  
24 role in the development of models for silicic magma degassing and volcanic eruptions. Found in  
25 most rhyolitic tephra deposits that are associated with domes or lavas (e.g. Rust et al., 2004; Castro et al.  
26 2014; Watkins et al. 2017, Gardner et al. 2017), these pyroclasts record a wide range of dissolved  
27 volatile contents, all of which are partially degassed relative to initial storage conditions (Taylor  
28 et al., 1983; Newman et al., 1988; Taylor, 1991; Watkins et al., 2017). This observation, combined  
29 with their low-to-zero vesicularity, was first explained by what became known as the “permeable  
30 foam model”, in which bubbly rhyolitic magma becomes permeable through partial bubble  
31 coalescence, allowing gases to escape and the remnant magma to collapse to a bubble-poor melt  
32 (Eichelberger et al., 1986; Jaupart and Allègre, 1991). This paradigm was linked to eruptive style,  
33 such that the collapse of the foam was postulated to cause the magma to effuse as degassed lava  
34 instead of erupting explosively (Eichelberger et al., 1986). More recent models have been  
35 proposed to explain the high dissolved volatile contents that appear inconsistent with the  
36 permeable foam model (e.g., Rust et al., 2004; Gonnermann and Manga, 2005a,b; Okumura et  
37 al., 2009; Cabrera et al., 2011; Castro et al., 2014). Textural evidence for brittle behavior in  
38 otherwise hot, viscous silicic magma has been used to implicate fracturing as the cause of open-  
39 system behavior (Tuffen et al., 2003; Tuffen and Dingwell, 2005; Cabrera et al., 2011), which in  
40 turn appears consistent with the style and extent of degassing recorded by dissolved volatiles  
41 (Rust et al., 2004; Castro et al., 2014). These models converge on the idea that brittleness  
42 resulting from high local strain rates in the melt lead to fractures that open the system, and that

43 this fracturing occurs repetitively (Tuffen et al., 2003) and pervasively (Castro et al., 2012) during  
44 magma ascent.

45 Gardner et al. (2017) re-examined obsidian pyroclasts from the North Mono eruption and  
46 found multiple lines of evidence that the obsidian is not collapsed foam. Instead, they proposed  
47 a model in which volcanic ash travelling up the conduit, above the fragmentation level, sticks to  
48 conduit walls and sinters to form low-porosity melt. Blebs of this melt are then reincorporated  
49 into the eruption to be deposited as glassy pyroclasts in the mainly pumiceous tephra. In this  
50 framework, variations in dissolved volatile concentrations represent differences in the depth at  
51 which ash sinters, and in the residence time at any given depth before final expulsion (Watkins  
52 et al., 2017; Gardner et al., 2017). An origin by in-conduit sintering explains the low porosity, the  
53 extent of open-system degassing of volatiles (Watkins et al., 2017), and trapped lithic fragments  
54 within obsidian pyroclasts (Rust et al., 2004; Gardner et al., 2017).

55 To explore the timescales involved in ash sintering, Gardner et al. (2018) experimentally  
56 subjected rhyolitic ash to temperatures and H<sub>2</sub>O pressures approximating those in the conduit.  
57 They found that ash-sized particles can equilibrate their dissolved volatile contents and sinter to  
58 vesicle-poor melt in as little as a few minutes, demonstrating that dense melt can form on the  
59 timescale of an eruption and thus obsidian pyroclasts need not be pieces of quenched magma  
60 emplaced before the eruption (cf. Newman et al., 1988; Dunbar and Kyle, 1992; Rust and  
61 Cashman, 2007).

62 The experimental results of Gardner et al. (2018) validated the timescales for sintering ash to  
63 obsidian, but they did not address the vesicle textures of obsidian pyroclasts. In fact, many  
64 textures of the North Mono obsidian pyroclasts do not match those predicted by isothermal

65 sintering. For example, sintered samples reach an equilibrium porosity of ~3–5 vol.%  
66 (Wadsworth et al., 2016; Gardner et al. 2018), which is thought to be the point at which  
67 permeability approaches zero, and porosity becomes isolated (Wadsworth et al., 2017).  
68 Although the value of 3 vol.% is in good agreement with predictions from percolation theory and  
69 simulations (Kertész 1981; Elam et al. 1984; Vasseur and Wadsworth, 2017), the majority of  
70 obsidian pyroclasts from the North Mono eruption have  $\leq 1$  vol.% vesicles, and some have no  
71 vesicles. Other textural variations in the natural samples include vesicles that range in shape  
72 from spherical to highly distorted, and in number densities ( $N_v$ ) between 0 (i.e., no vesicles) and  
73  $\sim 10^8$  vesicles per  $\text{cm}^3$  (Gardner et al., 2017). Volatile contents are also heterogeneous, regardless  
74 of vesicularity, and even very vesicle-poor obsidians have sub-domains with contrasting  $\text{H}_2\text{O}$  and  
75  $\text{CO}_2$  contents (Watkins et al., 2017).

76 Many textures seen in the North Mono obsidian pyroclasts were thus not captured by the  
77 experiments presented in Gardner et al. (2018) or indeed in any other experimental work  
78 designed to probe the origin of sintered rhyolitic deposits (Wadsworth et al., 2014). To address  
79 this gap we carried out sintering experiments that complement those of Gardner et al. (2018),  
80 but aim to replicate more accurately the natural scenario by using different particles sizes, mixed  
81 particle-size distributions, and by imposing cooling on the sintering particle pack. Combined,  
82 these results provide an improved framework in which to interpret the vesicle textures of  
83 obsidian pyroclasts.

84

## 85 **Methods**

86

87 All experiments used the same rhyolitic obsidian used by Gardner et al. (2018), the composition  
88 of which is listed in Table 1. This obsidian has a starting H<sub>2</sub>O concentration of 0.15 wt.%  
89 (Gardner et al. 2018). The obsidian was crushed into pieces with a steel mortar and pestle, and  
90 then those pieces were ground to a powder using an agate mortar and pestle. The powders  
91 were sieved at different times during the grinding process to produce splits of different particle  
92 sizes. The first split consisted of particles that remained on the no. 35 (500 μm) and no. 60 (250  
93 μm) mesh sieves. Because of their irregular shapes, the ash particles in this split have  
94 dimensions that are smaller and larger than 250–500 μm. We measured 20 random particles  
95 under the microscope and found that they had principal axes of 696±244 μm, 429±73 μm, and  
96 212±81 μm; we refer to this sample as “coarse ash”. The second split consisted of particles that  
97 passed through the no. 325 (45 μm) mesh sieve. Under the microscope we found that these  
98 are ≤2 to 45 μm in size; we refer to this sample as “fine ash”.

99 Separately, a cylindrical core was drilled from the obsidian, and hydrated at 875° C and 40  
100 MPa, following the methods of Gardner and Ketcham (2011). The resulting sample was clear  
101 rhyolitic glass with ~2.3 wt.% dissolved H<sub>2</sub>O, as measured by FTIR (see below). The glass was  
102 crushed, ground, and sieved, and we collected particles that remained on the no. 80 (180 μm)  
103 mesh sieve. Measurements of 20 random particles revealed that they are blockier than the  
104 coarse ash, with principal axes of 298±45 μm, 209±33 μm, and 159±25 μm; we refer to this  
105 sample as “wet ash”.

106 Each experiment used ~30–40 mg of powder (Table 1). In one set of experiments we used  
107 only one of the unimodal samples described above (fine, coarse, or wet). These experiments  
108 serve as a calibration of the sintering timescales for each population, before mixing

109 populations. In a second set of experiments, we used bimodal mixtures consisting of the fine  
110 ash mixed with either ~25 wt.% or ~50 wt.% coarse ash or 50 wt.% wet ash.

111 Each sample was weighed into a gold capsule (3 mm O.D.) that was welded shut on one  
112 end. The other end of the capsule was left open. Each capsule was placed into a sample holder  
113 at the end of an Inconel rod, which was then inserted into a pressure vessel fitted with a rapid  
114 quench extension, as described in Gardner (2007). The pressure vessel was connected to the  
115 pressure line, and 22 MPa of H<sub>2</sub>O pressure was applied. Because the capsule was open at one  
116 end, the pressurized H<sub>2</sub>O was in contact with the powder and thus the interstitial inter-  
117 connected pore space was at the same pressure as that in the pressure vessel. The capsule  
118 thus exerted no stress on the particles within, and the only stress driving sintering arose from  
119 interfacial tension between the molten particles and interstitial H<sub>2</sub>O (Gardner et al., 2018).

120 An external magnet held the sample rod in place, which held the sample inside a water-  
121 cooled jacket while the pressure vessel heated to 750°C, as measured by K-type thermocouples  
122 precise to ±5°C. When the vessel thermally equilibrated, pressure was set at ~2.0 MPa above  
123 22 MPa, as measured by a pressure transducer precise to ±0.1 MPa. The external magnet was  
124 then raised, lifting the sample into the hot zone of the pressure vessel in ~1 second; there was  
125 an associated pressure drop of ~2.0 MPa. Pressure was then quickly adjusted to 22 MPa in ~15  
126 seconds. The sample was held in place for 5 to 60 minutes (Table 1). During that time,  
127 pressure varied by no more than 0.1 MPa and temperature varied by no more than 1°C. After  
128 the target time was reached, the magnet was lowered, bringing the sample into the water-  
129 cooled jacket where it cooled at ~100°C per second (Gardner et al., 2018). When the sample

130 was lowered, pressure increased by  $\sim 2.0$  MPa, but was quickly adjusted back to 22 MPa in  $\sim 15$   
131 seconds.

132 In a final set of experiments, samples were sintered isothermally for a given time and then  
133 cooled slowly to a specified temperature before being quenched rapidly, to investigate the  
134 effects of cooling on final textures (Table 2). In this set of experiments, most samples consisted  
135 of fine ash – one held a 50:50 mix of fine and coarse ash – that were first held at 22 MPa and  
136  $750^\circ\text{C}$  for 5, 10, or 30 minutes, mimicking the isothermal experiments described above; the  
137 furnace was then switched off to allow the samples to cool. The rate of cooling changed with  
138 time, because it was controlled by the heat loss from the insulated furnace: it took  $49.6 \pm 5.7$   
139 seconds to cool from  $750^\circ\text{C}$  to  $748^\circ\text{C}$ , and then another  $36.2 \pm 3.9$  seconds to cool to  $745^\circ\text{C}$ .  
140 After that, samples cooled at an approximately constant rate of  $9.4 \pm 0.3^\circ\text{C}$  per minute, and the  
141 samples reached  $700^\circ\text{C}$  by  $6.3 \pm 0.3$  minutes,  $650^\circ\text{C}$  by  $11.4 \pm 0.6$  minutes, and  $550^\circ\text{C}$  by  $23.5 \pm 1.2$   
142 minutes. Although cooling slowed below  $650^\circ\text{C}$ , the change was not significant. Throughout  
143 cooling, pressure was maintained within 0.1 MPa of 22 MPa. All samples were quenched  
144 rapidly as soon as they reached the final target temperature.

145 Experiments were run over a range of temperatures from  $550^\circ$  to  $750^\circ\text{C}$  at 22 MPa.  
146 Assuming  $\text{H}_2\text{O}$  solubility (see below), those conditions equate to dissolved  $\text{H}_2\text{O}$  contents of 1.8  
147 to 2.2 wt.% (Liu et al., 2005). We estimate that melt viscosity was thus  $\sim 10^{7.1}$  to  $10^{10.1}$  Pa s  
148 (Hess and Dingwell, 1996), which is well below a viscosity of  $10^{11.4}$  Pa s that is typically  
149 considered for the glass transition (Gottsmann et al., 2002). Therefore, under all conditions of  
150 our experiments, the samples were fluid and could behave as melts.



151 All samples were extracted from their gold capsules and, if coherent, sealed in epoxy and  
152 thin sectioned to about 500  $\mu\text{m}$  thickness. A petrographic microscope was used to inspect  
153 sample textures and measure vesicle numbers, shapes, and sizes. Vesicle sizes were measured  
154 using a graduated ocular on the petrographic microscope, and are precise to  $\pm 0.5 \mu\text{m}$ . Number  
155 density of vesicles ( $N_V$ ) was measured by selecting different areas in a sample and counting all  
156 vesicles that appear as the field of view is moved through it using the focusing knob of the  
157 microscope;  $N_V$  is thus number density per unit total volume (melt plus vesicles). The depth  
158 viewed was measured using a Heidenhain focus drive linear encoder. All vesicles, regardless of  
159 shape, were counted, but only spherical vesicles were measured for size. Porosity ( $\phi$ ) was  
160 measured by photographing samples in reflected light, and then using NIH *Image J* to make  
161 binary images of the photographs to measure pore areas relative to the entire area of the  
162 image, and converted directly to porosity (vol.%). Errors on  $\phi$  are estimated at 10% of the  
163 measured value.

164 Glasses in the hydrated core, G-1724, G-1728, and G-1762 (Table 1) were analysed for  
165 dissolved  $\text{H}_2\text{O}$  contents by Fourier Transform Infrared (FTIR) spectroscopy in transmittance mode,  
166 using a Thermo Electron Nicolet 6700 spectrometer and Continuum IR microscope. Spectra were  
167 collected using 60 scans at a resolution of  $4 \text{ cm}^{-1}$ , and measured either in near-IR (7000 to 3800  
168  $\text{cm}^{-1}$ ) with white light and a  $\text{CaF}_2$  beamsplitter or in mid-IR (4000 to 650  $\text{cm}^{-1}$ ) with a globar source  
169 and KBr beamsplitter. Dissolved contents of molecular water ( $\text{H}_2\text{O}_m$ ) and hydroxyl water (OH)  
170 were determined from absorbances at  $\sim 5250 \text{ cm}^{-1}$  and  $\sim 4500 \text{ cm}^{-1}$ , respectively, using the model  
171 of Zhang et al. (1997), or from the broad absorbance at  $\sim 3500 \text{ cm}^{-1}$ , using an absorptivity of 75 L

172 mol<sup>-1</sup> cm<sup>-1</sup> (Okumura et al., 2003). Sample thickness where each spectrum was collected was  
173 determined using the method described above.

174 Area maps of OH, H<sub>2</sub>O<sub>m</sub>, and total H<sub>2</sub>O concentrations were made for G-1783 (Table 2) using  
175 a Thermo Nicolet Nexus 670 Fourier transform infrared (FTIR) spectrometer, following the  
176 methods of Watkins et al. (2017). All measurements were made using a 15X objective, infrared  
177 source, MCT-A detector, and KBr beamsplitter. Absorbances were converted to concentrations  
178 using the model of Zhang et al. (1997). The thickness of the sample was measured in several  
179 spots using a digital caliper with 0.001 mm precision. All spectra were collected at a resolution  
180 of 4 cm<sup>-1</sup>, 64 scans per spot, and 64 scans for the background, which was collected every 10  
181 minutes. Two maps were made, one using a 100 μm × 100 μm aperture and step size of 100 μm  
182 and the other a 40 μm × 40 μm aperture and step size of 40 μm. No significant differences were  
183 detected between the two maps.

184

## 185 **Experimental results**

186

### 187 Experiments Using Unimodal Powders

188

189 Post-experimental samples of sintered fine ash were all sufficiently coherent to section and  
190 analyze (Table 1). The highest measured porosity was ~46 vol.% for a sample that was  
191 incipiently sintered, which suggests that initial, unsintered porosity was slightly higher. This is  
192 consistent with the initial porosities measured by Gardner et al. (2018), who found that ash  
193 poured into capsules has an initial porosity between the particles of 45–55 vol.%, with less

194 polydisperse ash having higher porosity. Over run durations from 5 to 60 minutes, porosity  
195 decreased to the apparent equilibrium of ~3–5 vol.%, which was reached after 20 minutes  
196 (Figure 1). After 20 minutes, the sample of sintered fine ash (G–1728) has  $1.77 \pm 0.20$  wt.% H<sub>2</sub>O  
197 dissolved in the glass, which agrees well with the H<sub>2</sub>O content (1.81 wt.%) predicted by the  
198 model of Liu et al. (2005). Gardner et al. (2018) also found that dry ash fully saturated within  
199 20 minutes at 750°C and 40 MPa.

200 After 5 and 10 minutes, samples of sintered fine ash consist of completely open and  
201 connected pore space around individual ash particles that are still visible, although their edges  
202 have sintered to their closest neighbors, forming arcuate necks (Figure 2a). After 20 minutes,  
203 most pores are isolated from neighbors, but about two thirds of these vesicles are still  
204 distorted; the other third are spherical (Figure 2b,c). Between 30 and 60 minutes the  
205 proportion of distorted vesicles decreases significantly (Figure 2d), and by 60 minutes  
206 essentially all are spherical (Figure 2e). By 20 minutes, spherical vesicles are <2–5 μm in  
207 diameter but, later, larger ones become abundant. The larger vesicles did not grow from  
208 smaller ones, but instead result from large contorted vesicles taking longer to relax in shape.  
209 Values for  $N_V$  are  $\sim 10^{7.5-7.8} \text{ cm}^{-3}$  (Table 1).

210 Gardner et al. (2018) proposed a classification for the textural evolution of sintering  
211 unimodal rhyolitic ash, which identifies four phases: 1) particles are loose and lack cohesion; 2)  
212 particles are sintered at their contacts but are interpenetrated in a continuous, tortuous pore  
213 space; 3) porosity is no longer fully connected, with small isolated spherical vesicles and  
214 networks of larger vesicles that remain multi-cusped in shape; and 4) dense glass with fully  
215 isolated, spherical vesicles and maybe a few larger complex-shaped ones; duration of each

216 phase depends strongly on melt viscosity. We use this framework to present the results of  
217 these experiments with unimodal samples, finding that the textures of the sintered fine ash  
218 follow the same progression (Figure 3). Samples sintered for 5 and 10 minutes consist of  
219 individual particles partially sintered in open pore space (Phase 2). Between 20 and 45 minutes,  
220 samples have low porosities, but distorted vesicles make up 40 to 70% of the population (Phase  
221 3). After sintering for 60 minutes the sample consists of dense glass with only spherical vesicles  
222 (Phase 4).

223 The two experiments using only coarse ash were run for 30 and 60 minutes, but remained  
224 unsintered and crumbled to loose powder on extraction from the capsules, implying that the  
225 inter-particle porosity did not decrease much below the initial value and the samples remained  
226 in Phase 1. The two experiments using only wet ash were coherent enough to section, and  
227 both consist of individual ash particles that are only slightly sintered along their edges (Figure  
228 2f). The particles are dispersed amongst an open and connected pore space that makes up 30–  
229 35 vol.% of the samples (Figure 1). The wet ash samples thus remained in Phase 2 of textural  
230 evolution even after 60 minutes.

231

#### 232 Experiments Using Bimodal Mixed Ash Populations

233

234 In all mixed-ash samples, even when sintering has progressed significantly – which normally  
235 removes evidence of individual particles – the coarse or wet ash component can still be  
236 recognized as large non-vesicular domains, and in the case of wet ash as microlite-free

237 domains. Overall, bimodal samples sinter more slowly, as measured by the evolution of  
238 porosity, than samples that consisted of only fine ash (Figure 1).

239 In describing the final textures of the mixed-ash samples, we use *matrix* to refer to domains  
240 that initially consisted of fine ash between areas that were initially either coarse or wet  
241 particles. When coarse ash makes up half of the sample, the matrix after 20 minutes (G-1724)  
242 consists of small ash particles that are slightly sintered surrounded by ~33 vol.% of pore space  
243 (Figure 4a). Pockets of large vesicles occur in the matrix that can be  $\geq 800$  microns in size, with  
244 most pockets found in the vicinity of relict large particles. FTIR measurements show that the  
245 large relicts have 0.57–1.79 wt.% H<sub>2</sub>O dissolved in them (measured in the interiors of large  
246 particles, as far away from the edges as possible), which is below the solubility value of 1.81  
247 wt.% (Liu et al., 2005). After 45 minutes, matrix porosity is still heterogeneous, and depends on  
248 proximity to relict coarse particles (Figure 4b,c). Where coarse particles are closer together than  
249 ~200  $\mu\text{m}$ , the matrix is of the order of 26 vol.% porous and can preserve pockets of large  
250 vesicles up to 600  $\mu\text{m}$  long; where farther apart, the matrix is only about 4 vol.% porous. In  
251 both regions,  $N_V \sim 10^{7.2} \text{ cm}^{-3}$  and the vast majority of vesicles are distorted and connected  
252 together via narrow channels. After 60 minutes, the matrix is almost uniformly dense, and  
253 large pockets of vesicles are rarer and  $\leq 200 \mu\text{m}$  in size (Figure 4d). All vesicles are isolated, but  
254 only about half are spherical. The dissolved H<sub>2</sub>O contents in the interiors of the relict coarse  
255 particles is 1.84 ( $\pm 0.14$ ) wt.%, which is within error of the 1.81 wt.% saturation limit of H<sub>2</sub>O (Liu  
256 et al., 2005).

257 A similar progression of textures is observed when coarse ash makes up only ~25 wt.% of  
258 the sample, except that matrix porosity is lower after any given amount of time (Figure 1).

259 Relatively large porous pockets still exist, but they are generally smaller and few remain after  
260 45 minutes. One experiment that contained fine ash and 50 wt.% wet ash was run for 20  
261 minutes. Its matrix is similar in porosity to that of the coarse ash mix that sintered for more  
262 than twice as long (Figure 1). It contains large pockets of vesicles up to 300  $\mu\text{m}$  long and mainly  
263 highly contorted, multi-cusped vesicles; only about 16% of the vesicles are spherical.

264 Overall, the temporal evolution of textures in the mixed-ash populations is broadly similar  
265 to the unimodal case for fine ash, such that porosity generally decreases with time and the end-  
266 state is isolated vesicles (Figure 1). The presence of large particles, however, slows the rate of  
267 decrease in porosity, and causes individual vesicles to take longer to relax to spherical. After 60  
268 minutes, for example, 13–20% of the matrix vesicles are still distorted in samples with 50%  
269 coarse particles, whereas all were spherical in samples of fine ash only. Another important  
270 difference is that bimodal samples produce textures that are considerably more  
271 heterogeneous, with pockets of large vesicles. These pockets generally decrease in size with  
272 time, and are less abundant when coarse particles are less abundant.

273

#### 274 Experiments Combining Sintering and Cooling

275

276 Six samples of fine ash were cooled slowly after sintering at 750°C (Table 2). All have  
277 significantly reduced porosities compared to samples that were not slowly cooled (Figure 5).  
278 For example, sintering isothermally for 5 minutes produced only incipiently sintered particles  
279 amongst ~45 vol.% connected pore space, whereas subsequent cooling to 550°C produced  
280 dense glass with 7 vol.% isolated vesicles. Importantly, cooling is found to be able to produce

281 dense glass with no measurable vesicles (Figure 5), and reduced  $N_v$  from  $10^{7.66} \text{ cm}^{-3}$  to zero  
282 vesicles (Table 2). FTIR Mapping across G-1783 (no vesicles present) found H<sub>2</sub>O concentrations  
283 between 1.88 and 2.16 wt.%, averaging  $2.03 \pm 0.06$  wt.%. That range falls between solubility  
284 H<sub>2</sub>O concentrations expected at 750° to 550°C and 22 MPa (Liu et al., 2005).

285 Although porosity is reduced during cooling, the preserved vesicles are relatively more  
286 deformed than those found after similar durations at high temperature. For example, after 30  
287 minutes of sintering at 750°C (G-1729) about half of the vesicles have relaxed to spherical  
288 shape (Figure 6a). In contrast, G-1789, which sintered for 10 minutes at 750°C and then cooled  
289 to 550°C for ~25 minutes (total time = 35 minutes), has the same porosity, but all of the vesicles  
290 are distorted in shape (Figure 6b). Cooling can thus prolong the time it takes for distorted  
291 vesicles to relax to spherical, while simultaneously reducing overall porosity.

292 One sample that consisted of equal proportions of fine and coarse ash was cooled to 650°C  
293 after sintering for 30 minutes (G-1785; Table 2). Given the total amount of time spent at  
294 elevated temperature (41 minutes), this sample would be expected to have a porosity of ~3  
295 vol.% far from large particles and ~26 vol.% near relict particles (compared to G-1760; Table 1).  
296 Instead, the corresponding values for the cooled sample are ~2 and ~16 vol.%. Furthermore,  
297 cooling reduced  $N_v$  by an order of magnitude compared with the isothermal sample (Tables 1  
298 and 2).

299

## 300 **Analysis of Experimental Results**

301

302 The textural descriptions above highlight some of the complexities of the sintering process for  
303 rhyolitic particles that have not been accounted for in existing sintering models (Wadsworth et  
304 al., 2014; 2016). Here, we place these experiments in the context of existing theoretical  
305 constraints to highlight these differences.

306 Gardner et al., (2018) defined two timescales relevant to sintering of unimodal rhyolite  
307 particles that were also hydrating. The first timescale is for diffusive hydration ( $\lambda_d$ ), during  
308 which the dissolved H<sub>2</sub>O content increases from the initial value of 0.15 wt.% to the saturation  
309 value, which depends on the sintering temperature and pressure. The second timescale is for  
310 sintering ( $\lambda_s$ ). For randomly packed, monodisperse spherical particles (droplets when molten),  
311 the sintering timescale is given by

312

$$313 \quad \lambda_s = \frac{\eta L}{\sigma} \quad (1)$$

314

315 where  $\eta$  is droplet viscosity (Pa s),  $\sigma$  is surface tension (N m<sup>-1</sup>), and  $L$  (m) is a characteristic  
316 length scale, which can be approximated as the mean particle radius ( $\bar{R}$ ) in the case of sintering  
317 angular particles (Gardner et al., 2018). The diffusive hydration timescale is given by

318

$$319 \quad \lambda_d = \frac{\bar{R}^2}{D} \quad (2)$$

320

321 where  $D$  is the diffusivity of H<sub>2</sub>O in rhyolite. Both  $\eta$  and  $D$  are material properties that must be  
322 computed from constitutive models. We use the model of Hess and Dingwell (1996) to  
323 compute  $\eta$  as a function of dissolved H<sub>2</sub>O concentration ( $C$ ) and temperature ( $T$ ). In turn, we



324 use the model of Liu et al. (2005) to compute  $C$  at isothermal temperature ( $T_0$ ) and isobaric  
325 pressure ( $P_0$ ). We use the model of Zhang and Ni (2010) to compute  $D$ , as a function of  $C$ ,  $T_0$ ,  
326 and  $P_0$ . We set  $\sigma = 0.22 \text{ N m}^{-1}$ , following Gardner et al. (2018) for the same starting material.

327 Comparing timescales yields the dimensionless capillary Peclet number ( $P_c$ ) =  $\lambda_d/\lambda_s$   
328 (Gardner et al., 2018). For  $\lambda_d \ll \lambda_s$  (i.e.,  $P_c \ll 1$ ) diffusive hydration occurs rapidly compared  
329 with sintering. Conversely, for  $\lambda_d \gg \lambda_s$  (i.e.,  $P_c \gg 1$ ) sintering occurs rapidly compared with  
330 diffusive hydration. Because both timescales depend on  $C$ , and  $C$  changes over time during the  
331 experiments, we need to establish what value of  $C$  to use to compute the timescales. We  
332 assume that the particles have equilibrium  $\text{H}_2\text{O}$  concentrations ( $C_e$ ) for  $P_c \ll 1$ , and the  
333 particles have their initial  $\text{H}_2\text{O}$  concentrations for  $P_c \gg 1$ . Gardner et al. (2018) found that  
334 sintering can be assumed to be proceeding at equilibrium conditions as long as  $P_c \lesssim 10$  (the  
335 low  $P_c$  regime). All unimodal experiments of this study meet the condition  $P_c < 10$ , implying  
336 that hydration was complete before sintering. This is confirmed by measurements of  $\text{H}_2\text{O}$   
337 concentration in G-1728 (measured for experimental conditions where time  $> \lambda_d$ ), which is  
338 within uncertainty of  $C_e$ . We thus assume  $C_e$  has been reached, and use that value to compute  
339 the viscosity at  $C_e$  (which we term  $\eta_e$ ) in (1) to predict  $\lambda_s$ .

340 The metric most commonly used to track the progression of sintering is the interstitial  
341 porosity ( $\phi$ ) to the particles (Wadsworth et al., 2014; 2016). Wadsworth et al. (2016) found an  
342 analytical approximation of a full sintering model that can be used to predict the porosity of a  
343 random pack of particles as a function of time ( $t$ ) following

344

345 
$$\phi(t) = \phi_i \exp\left(-\frac{3t}{2\lambda_s}\right). \quad (3)$$

346

347 This expression has been validated for angular particles (Gardner et al., 2018; Wadsworth et al.,  
348 2014). We find that the predicted  $\phi(t)$  curve computed using (3), with  $\lambda_s$  computed from (1),  
349 agrees well with the unimodal data using very different ash sizes as starting materials (Figure 7).  
350 Note, initial porosity is taken as  $\phi_i = 45$  or  $60$  vol.%, and there are no adjustable parameters.

351 In the case of bimodal experiments, which contained two different  $\bar{R}$  values in different  
352 proportions, the sintering process is complicated because the values of  $\lambda_d$  are different for each  
353 constituent particle size class in the mixed population. This means that there can be conditions  
354 for which  $t < \lambda_d$  for large particles, while  $t > \lambda_d$  for small particles. This is illustrated by the  
355 cores of coarse particles in G-1724 having measured H<sub>2</sub>O concentrations that is just over half of  
356  $C_e$ , whereas, after the same amount of time, unimodal fine ash in G-1728 is fully hydrated. The  
357 result of this is that a system can be sintering particles with very different viscosities. Despite  
358 such complexities, we found that the porosity of any bimodal mixture is intermediate, although  
359 heterogeneous, between predicted values for  $\phi(t)$  of the end-member unimodal  $\bar{R}$  classes  
360 (Figure 7). In addition, the bimodal experiments that contain proportionally more fine ash  
361 sintered faster, and hence approached the equilibrium porosity faster. While a full predictive  
362 model for bimodal (and polymodal) sintering is beyond the scope of this study, we suggest that  
363  $\phi(t)$  for bimodal sintering populations can be qualitatively estimated from those of the end-  
364 member populations.

365

366 Resorption of Isolated Vesicles During Cooling

367

368 Assuming that the cooled samples and isothermal samples initially had similar textures before  
369 the start of the cooling ramp, our experiments demonstrate that slow cooling causes vesicles to  
370 shrink and disappear (Figure 8). We hypothesize that this is caused by thermally-driven  
371 resorption of H<sub>2</sub>O; i.e., the increase in H<sub>2</sub>O solubility with decreasing  $T$  is sufficient to cause all  
372 H<sub>2</sub>O in the bubbles to resorb into the surrounding melt. McIntosh et al (2014) first proposed  
373 that this mechanism could play a role in the formation of dense obsidian.

374 For bubbles to resorb completely, there must be sufficient time for all H<sub>2</sub>O molecules within  
375 the bubbles to diffuse into the surrounding melt. There must also be enough time for the melt  
376 to flow viscously to allow the bubbles to shrink. To determine whether this is feasible in the  
377 experiments, we compare three timescales: (1) the time available for diffusion and flow,  $\lambda_a$ ; (2)  
378 the time that would be required for H<sub>2</sub>O to resorb diffusively,  $\lambda_\gamma$ ; and (3) the time that would  
379 be required for the melt to flow,  $\lambda_\eta$ . To test the resorption hypothesis, we determine these  
380 three timescales for sample G-1783 (Table 2).

381 For this analysis, the time available for the bubble to resorb,  $\lambda_a$  is taken simply as the  
382 duration of the cooling ramp. We derive order-of-magnitude estimates for the time required  
383 for diffusion,  $\lambda_\gamma$ , and viscous flow,  $\lambda_\eta$ , in Appendix A. We find that the time required for  
384 diffusion to resorb all of the water in the bubbles depends strongly on the initial size of the  
385 bubble, while the time required for viscous flow to allow the bubble to collapse depends only  
386 weakly on the initial bubble size. In Figure 8,  $\lambda_\gamma$  and  $\lambda_\eta$  are plotted (solid and dash line  
387 respectively) as functions of initial bubble radius, given  $P_o = 22$  MPa and  $T_o = 750^\circ\text{C}$ . The time  
388 available for diffusion and flow ( $\lambda_a$ ) is also plotted for both the cooling ramp (red line), and for

389 rapid quench (blue line). We find that, over the range of initial bubble sizes in our experiments  
390 (indicated by the grey box), the time available for resorption during slow cooling is longer than  
391 the diffusion and flow timescales, hence there is sufficient time for resorption to go to  
392 completion. In contrast, the time available for resorption during rapid cooling is shorter than  
393 both the diffusion and flow timescales, hence there is insufficient time for resorption. This  
394 supports our hypothesis that thermally driven resorption is sufficient to cause the complete  
395 removal of the bubbles during slow cooling (Figure 5).

396 To first order, therefore, we find that slow cooling of porous rhyolitic melt can cause H<sub>2</sub>O  
397 pores to resorb and produce porosities lower than the equilibrium sintering value of 3–5 vol.%.  
398 We note, however, that our approach (Appendix A) to determine order-of-magnitude values for  
399  $\lambda_\gamma$  and  $\lambda_\eta$  is highly simplified. We thus caution against using this approach to make  
400 quantitative predictions about the conditions under which resorption may occur in natural  
401 systems. While such predictions are possible, it would require a numerical approach that is  
402 beyond the scope of this work.

403

## 404 **Discussion**

405

406 Our sintering experiments, combined with those of Gardner et al. (2018), place constraints on  
407 the formation of vesicle textures generated during sintering. Comparing those results to  
408 textures of natural obsidian pyroclasts provides a framework for understanding how the  
409 pyroclasts form. All experiments show that, as ash sinters, the volume of open pore space  
410 decreases and is sealed off, generating isolated vesicles (Figure 3). Those vesicles start off

411 highly distorted and convolute, but eventually relax to spherical shapes (Figure 2). That  
412 sequence occurs in the different sets of experiments, but the timescales for sintering and  
413 vesicle relaxation depend strongly on viscosity and initial particle size (Wadsworth et al., 2014;  
414 Gardner et al., 2018; this study). The general progression from distorted to spherical shapes  
415 observed in the experiments supports the overall premise of the model proposed by Gardner et  
416 al. (2017) for the formation of obsidian pyroclasts in the North Mono eruption. They suggested  
417 that the main mechanism for the formation of these pyroclasts is sintering of volcanic ash in the  
418 conduit, speculating that vesicles start out distorted in shape but relax to spherical with time.  
419 Furthermore, the experiments demonstrate that distorted and spherical vesicles may coexist  
420 (i.e., Phases 2–3) during the sintering process, as observed in North Mono obsidian pyroclasts  
421 (Figure 9a).

422 Our experiments show that sintering unimodal ash evolves texturally towards  
423 homogeneously distributed spherical vesicles (Figure 2e). About 10–15% of the North Mono  
424 obsidian pyroclasts studied by Gardner et al. (2017) contain only spherical vesicles (Figure 9b;  
425 see also Figure 5a in Gardner et al., 2017). We infer that those obsidian pyroclasts preserve the  
426 end products of sintering unimodal distributions of ash. Experimental sintering of unimodal ash  
427 also shows that  $N_v$  is related to the size distribution of particles sintered. Sintering of fine ash  
428 ( $\leq 45 \mu\text{m}$ ; this study) produced  $N_v = 10^{7.51 \pm 0.19} \text{ cm}^{-3}$  (Table 1). Sintering of ash that ranged in size  
429 by 1–1600  $\mu\text{m}$  ( $\bar{R} = 89 \mu\text{m}$ ) resulted in  $N_v = 10^{6.55 \pm 0.23} \text{ cm}^{-3}$  (Gardner et al., 2018). Sintering of  
430 coarser but less polydispersive ash of  $\sim 63$ –400  $\mu\text{m}$  in size ( $\bar{R} = 185 \mu\text{m}$ ) produced even fewer  
431 vesicles,  $N_v = 10^{5.62 \pm 0.19} \text{ cm}^{-3}$  (Gardner et al., 2018). The differences in  $N_v$  are significant,  
432 representing one to two orders of magnitude variation in numbers of vesicles within a given

433 volume. Vesicles in North Mono obsidian pyroclasts occur in  $N_v$  values from 0 (no vesicles) to  
434  $10^{8.1} \text{ cm}^{-3}$ , but more than half have  $N_v > 10^{6.8} \text{ cm}^{-3}$  (Gardner et al., 2017).

435 We propose that North Mono obsidian pyroclasts with abundant vesicles formed by  
436 sintering fine-grained ash. Fine-grained ash in fact makes up a large fraction of tephra  
437 produced in explosive eruptions (Walker, 1981; Kaminski and Jaupart, 1998; Bonnadonna and  
438 Houghton, 2005; Alfano et al., 2016). If the fine ash is approximately unimodal, we show that  
439  $\phi(t)$  can be predicted, and Gardner et al. (2018) provide a full framework for estimating it at  
440 conduit conditions.

441 The majority of North Mono obsidian pyroclasts have <1 vol.% porosity; furthermore, 3 of  
442 81 samples reported by Gardner et al. (2017) were entirely vesicle-free. Experimental sintering  
443 of unimodal ash, in contrast, typically produces an equilibrium texture of 3–5 vol.% vesicles  
444 (Figure 1; Wadsworth et al., 2014; Gardner et al., 2018). The cause of this discrepancy has  
445 remained enigmatic until now. Our experiments suggest that the relatively low porosities of  
446 the natural obsidians result from resorption induced by cooling during sintering, and the  
447 associated increase in  $\text{H}_2\text{O}$  solubility in the melt (Figure 8). We posit that many of the North  
448 Mono obsidian pyroclasts thus preserve a record of cooling during sintering. In support of this,  
449 our results show that non-spherical vesicle shapes can be preserved during cooling, and may  
450 remain abundant well below the equilibrium porosity of 3–5 vol.% (Figure 6). Very poorly  
451 vesicular North Mono obsidian pyroclasts, in fact, contain vesicles of all shapes, including highly  
452 distorted ones (Figure 9c,d). Only a small minority of North Mono obsidian pyroclasts are free  
453 of vesicles, which suggests that the time available for cooling was relatively short. Indeed, the

454 overall timescale for formation of obsidian pyroclasts as deduced from diffusion modelling of  
455 volatile gradients is less than a few hours (Watkins et al., 2017).

456 It thus appears that some vesicle textures in natural obsidian pyroclasts can be explained by  
457 sintering of unimodal ash, and that variations in textures among such pyroclasts are the result  
458 of variations in starting particle sizes and in the cooling rate. There are other textural features  
459 common to obsidian pyroclasts that are not replicated by experimental sintering of unimodal  
460 ash, such as significant spatial heterogeneities in vesicles and volatile contents within a single  
461 pyroclast (Rust et al., 2004; Rust and Cashman, 2007; Castro et al., 2014; Watkins et al., 2017;  
462 Gardner et al., 2017). These include large pockets of vesicles dispersed amongst poorly  
463 vesicular, dense glass (Figure 9d) and regions of poorly vesicular glass separated by glass with  
464 numerous vesicles (Figure 9c,e,f). Many of these vesicular heterogeneities coincide with  
465 heterogeneous dissolved volatile concentrations (Watkins et al., 2017).

466 We suggest that the spatial heterogeneities in vesicles and volatiles within obsidian  
467 pyroclasts result from sintering of particles of differing size, based on our results of sintering of  
468 mixed-ash populations. We found that large scale heterogeneities in vesicles can occur when  
469 samples consist of mixed ash particles (Figure 4). For example, sintering of coarse and fine ash  
470 produced regions poor in vesicles (large relict particles) separated by porous bands of matrix  
471 (Figure 4e). Sintering of mixed ash samples also resulted in sub-domains of matrix with large  
472 pockets of vesicles (Figure 4b,f), which are reminiscent of isolated clusters of large vesicles in  
473 the natural obsidian pyroclasts (Figure 9e).

474 The degree of heterogeneity is likely related to the contrast in sizes between sintering  
475 particles. In this study, bimodal populations resulted in highly vesicular bands separating

476 relatively large, non-vesicular regions (Figure 4c,e). When the sintering pack includes a wide  
477 range of particle sizes, then heterogeneities in vesicular textures range in size reflecting the  
478 particle sizes (Gardner et al., 2018). Our results additionally suggest that heterogeneities in  
479 volatile contents will result when the residence time at a given  $T$  and  $P$  is sufficient to  
480 homogenize small particles ( $t < \lambda_d$ ) but not sufficient to homogenize large ones ( $t > \lambda_d$ ).  
481 Commonly, the large, poorly vesicular domains in the North Mono obsidian pyroclasts are H<sub>2</sub>O–  
482 rich relative to the vesicular domains (Watkins et al., 2017). We suggest that they are pieces of  
483 glass formed by sintering and cooling of ash that was then ripped off of the conduit walls, only  
484 to be re-plastered onto the walls and sinter with adjoining ash.

485 Finally, a prominent texture of North Mono obsidian pyroclasts not replicated in any sintering  
486 experiment so far is stretched/elongated vesicles (see Figures 5c,d and 6d,f in Gardner et al.,  
487 2017). Such stretched vesicles usually align with their neighbors, implying that they formed by  
488 shearing of distorted or spherical vesicles (Gardner et al., 2017). No shear occurred in our  
489 experiments because the applied pressure is isotropic. Over 70% of the North Mono obsidians  
490 preserve stretched/elongated vesicles, indicating that most, if not all, pyroclasts underwent  
491 shearing during their formation. It is not possible to determine the cause of shearing based on  
492 available evidence, but we speculate that it could be associated with gravitational slumping of  
493 the sintering mass at the conduit wall or shearing along the margins induced by the ascent of the  
494 adjacent erupting gas–particle dispersion, either before or during the disruption of the obsidian  
495 to form pyroclasts.

496

497 **Conclusions**



498

499 Rhyolitic ash particles were experimentally sintered to examine the evolution of the vesicle  
500 textures that result. Results show that, regardless of particle size, porosity decreases with time  
501 and the interstitial pores quickly isolate to form vesicles amongst the sintering particles. With  
502 time, isolated vesicles that are initially highly distorted relax to spherical shapes. The rates of  
503 sintering and relaxation depend on melt viscosity and initial sizes of the particles. All else being  
504 equal, smaller particles sinter more quickly than coarser ones. We also found that high vesicle  
505 number densities ( $N_v \geq 10^7 \text{ cm}^{-3}$ ) and generally small vesicle sizes result when the sintering  
506 particles are unimodal fine-grained ash. Cooling of the sintering pack causes thermally-driven  
507 resorption of volatiles, which reduces vesicle abundances below the equilibrium abundance of  
508 3–5 vol.%, and can ultimately produce glass that is devoid of vesicles. While cooling reduces  
509 the overall porosity, it also allows distorted vesicles to be preserved for longer periods of time,  
510 and to lower porosities. Finally, bimodal mixtures of coarse and fine ash result in significantly  
511 more heterogeneous vesicular textures than unimodal samples, including the creation of large  
512 pockets of large vesicles between relict coarse particles. In addition, the overall reduction of  
513 porosity and relaxation of vesicle shapes also takes longer than in unimodal samples.

514 These results provide a framework in which to interpret observed vesicle textures in natural  
515 obsidian pyroclasts. In general, we conclude that obsidian pyroclasts form by sintering of  
516 mostly fine-grained ash on conduit walls. The sintering ash also cools sufficiently slowly that  
517 the majority of obsidian pyroclasts have vesicle abundances well below those produced in  
518 isothermal sintering experiments. The various scales of heterogeneous vesicle abundances and  
519 volatile concentrations indicate that the sintering particle pack is not only unimodal fine ash

520 and that some pieces of obsidian incorporated by the eruption column are re-plastered onto  
521 the walls to re-sinter with other fragments and more ash.

522

### 523 **Acknowledgements**

524 JEG and JMW were partially supported by grants from the National Science Foundation (EAR–  
525 1725186 and EAR–1725207). EWL and JPC acknowledge support from the UK Natural  
526 Environment Research Council via grant NE/N002954/1. FBW acknowledges a fellowship from  
527 the Centre for Advanced Study at the Ludwig-Maximilians-Universität, Munich. All data from  
528 the study can be obtained from JEG. The authors thank two anonymous reviewers and the  
529 Associate Editor for their insights, which have improved the manuscript.

530

### 531 **Appendix A**

532

533 Whether there is enough time for silicate melt to flow viscously to allow the bubbles to shrink  
534 depends on the timescale for H<sub>2</sub>O to resorb from vesicles ( $\lambda_\gamma$ ) and the characteristic time  
535 required for the melt to flow ( $\lambda_\eta$ ). Both timescales are functions of solubility ( $C_e$ ), diffusivity  
536 ( $D$ ), and melt viscosity ( $\eta$ ), all of which are functions of temperature (Figure A1), and so they  
537 change through the cooling ramp. The curves for  $C_e(T)$  and  $D(T)$  also require a dissolved water  
538 content to be assumed. We choose  $C_{e,0}$ , which is the initial solubility of water in the melt, in  
539 wt.%, at the start of the cooling ramp. This is the lowest dissolved water content anticipated  
540 during the experimental run. This value yields the highest viscosity and slowest diffusivity, and  
541 so constitutes the most conservative assumption. In our analysis we use the time-averaged  
542 values of each parameter over the linear cooling ramp:  $\overline{C_e}$ ,  $\overline{D}$ , and  $\overline{\eta}$  respectively.

543 In order to estimate  $\lambda_\gamma$  we first calculate the mass ( $M_0$ ) of H<sub>2</sub>O contained within a bubble of  
544 initial radius ( $R_0$ ) at the start of the cooling ramp, using the equation of state of Pitzer and

545 Sterner (1994). We then calculate the volume ( $V$ ) of melt that would be required to resorb this  
 546 mass of water:

547

$$548 \quad V = \frac{M_0(R_0, P, T_0)}{\left[ \frac{(C_e - C_{e,0})}{100} \rho_m \right]}, \quad (\text{A1})$$

549

550 where  $M_0(R_0, P, T_0)$  indicates that  $M_0$  is a function of initial bubble radius, experimental  
 551 pressure, and initial temperature (via the equation of state), and  $\rho_m$  is density of the melt,  
 552 taken as  $2300 \text{ kg m}^{-3}$ . We assume that, if resorption goes to completion, then  $V$  will be a sphere  
 553 of hydrated melt with radius  $R_h = \sqrt[3]{3V/4\pi}$ . The characteristic diffusion length scale at the  
 554 end of the cooling ramp is estimated as  $l_D = \sqrt{Dt}$ . By setting  $l_D = R_h$ , we can estimate the  
 555 duration of the cooling ramp required to fully resorb the water in the bubble by diffusion:

556

$$557 \quad \lambda_\gamma = \frac{1}{D} \left( \frac{3M_0(R_0, P, T_0)}{4\pi\rho_m \frac{(C_e - C_{e,0})}{100}} \right)^{\frac{2}{3}}. \quad (\text{A2})$$

558

559 The characteristic time required for the melt to flow viscously to allow the bubble to collapse is  
 560 estimated by assuming that it scales with the ratio of the viscosity of the melt to the stresses  
 561 driving collapse, which are the surface tension (Laplace) stress  $\sigma$  and the confining pressure,  
 562 given by

563

$$564 \quad \lambda_\eta = \frac{\bar{\eta}}{\left( \frac{\sigma}{R_0} + P_0 \right)}. \quad (\text{A3})$$

565

566

567 **Figure A–1:** Solid curves are solubility ( $C_e$ ), diffusivity ( $D$ ), and viscosity ( $\eta$ ) as functions of  
568 temperature, all at 22 MPa H<sub>2</sub>O pressure. Dash lines are time-averaged values of each  
569 during constant rate cooling from 750°C to 550°C. Diffusivity and viscosity are calculated  
570 under the conservative assumption that dissolved H<sub>2</sub>O content is given by solubility at  
571 750°C.

572

573 **References**

- 574 Alfano, F., Bonadonna, C., Watt, S., Connor, C., Volentik, A., and Pyle, D.M., 2016. Reconstruction  
575 of total grain size distribution of the climactic phase of a long-lasting eruption: the example  
576 of the 2008–2013 Chaitén eruption. *Bull. Volcanol.* 78, 46.
- 577 Bonadonna, C., and Houghton, B.F., 2005. Total grain-size distribution and volume of tephra-fall  
578 deposits. *Bull. Volcanol.* 67(5), 441-456.
- 579 Cabrera, A., Weinberg, R.F., Wright, H.M.N., Zlotnik, S., and Cas, R.A.F., 2011. Melt fracturing and  
580 healing: A mechanism for degassing and origin of silicic obsidian. *Geology* 39, 67-70.
- 581 Castro, J.M., Cordonnier, B., Tuffen, H., Tobin, M.J., Puskar, L., Martin, M.C., (2012) The role of  
582 melt-fracture degassing in defusing explosive rhyolite eruptions at Volcán Chaitén. *Earth  
583 Planet Sci Lett* 333-334, 63-69.
- 584 Castro, J. M., Bindeman, I. N., Tuffen, H., and Schipper, C. I., 2014. Explosive origin of silicic lava:  
585 textural and  $\delta D-H_2O$  evidence for pyroclastic degassing during rhyolite effusion. *Earth Planet.  
586 Sci. Lett.* 405, 52-61.
- 587 Dunbar, N.W., and Kyle, P.R., 1992. Volatile contents of obsidian clasts in tephra from the Taupo  
588 Volcanic Zone, New Zealand: Implications to eruptive processes. *J. Volcanol. Geotherm. Res.*  
589 49, 127-145.
- 590 Eichelberger, J.C., Carrigan, C.R., Westrich, H.R., and Price, R.H., 1986. Non-explosive silicic  
591 volcanism. *Nature* 323, 598–602.
- 592 Elam, W.T., Kerstein, A.R. and Rehr, J.J., 1984. Critical properties of the void percolation  
593 problem for spheres. *Physical review letters*, 52(17), p.1516.
- 594 Gardner, J.E., 2007. Bubble coalescence in rhyolitic melts during decompression from high  
595 pressure, *J. Volcanol. Geotherm. Res.*, 166, 161-176.
- 596 Gardner, J.E., and R.A. Ketcham, 2011. Bubble nucleation in rhyolite and dacite melts:  
597 Temperature dependence of surface tension. *Contrib. Mineral. Petrol.* 162, 929-943.
- 598 Gardner, J.E., Llewellyn, E.W., Watkins, J.M., and Befus, K.S., 2017. Formation of obsidian  
599 pyroclasts by sintering of ash particles in the volcanic conduit. *Earth Planet. Sci. Lett.* 459,  
600 252-263.
- 601 Gardner, J.E., Wadsworth, F.B., Llewellyn, E.W., Watkins, J.M., and Coumans, J.P., 2018.  
602 Experimental sintering of ash at conduit conditions and implications for the longevity of  
603 tuffisites. *Bull. Volcanol.* 80, 23.
- 604 Gonnermann, H. M., Manga, M., 2005a, Nonequilibrium magma degassing: results from  
605 modeling of the ca. 1340 AD eruption of Mono Craters, California. *Earth and Planetary  
606 Science Letters*, v. 238, no. 1, p. 1–16.
- 607 Gonnermann, H. M., Manga, M., 2005b, Flow banding in obsidian: A record of evolving textural  
608 heterogeneity during magma deformation, *Earth and Planetary Science Letters*, v. 236, no.  
609 1, p. 135–147.
- 610 Gottsmann, J., Giordano, D. and Dingwell, D.B., 2002. Predicting shear viscosity during volcanic  
611 processes at the glass transition: a calorimetric calibration. *Earth and Planetary Science  
612 Letters*, 198(3-4), pp.417-427.
- 613 Hess, K.-U., and Dingwell, D.B., 1996. Viscosities of hydrous leucogranitic melts: A non-Arrhenian  
614 model. *Am. Mineral.* 81, 1297–1300.

615 Jaupart, C., and Allegre, C.J., 1991. Gas content, eruption rate and instabilities of eruption regime  
616 in silicic volcanoes. *Earth Planet. Sci. Lett.* 102, 413–429.

617 Kaminski, E., and Jaupart, C., 1998. The size distribution of pyroclasts and the fragmentation  
618 sequence in explosive volcanic eruptions. *J. Geophys. Res.* 103(B12), 29759-29779.

619 Kertész, J., 1981. Percolation of holes between overlapping spheres: Monte Carlo calculation of  
620 the critical volume fraction. *Journal of Physique Lettres*, 42(17), 393–395.  
621 doi: 10.1051/jphyslet:019810042017039300

622 Liu, Y., Zhang, Y., and Behrens, H., 2005. Solubility of H<sub>2</sub>O in rhyolitic melts at low pressure and a  
623 new empirical model for mixed H<sub>2</sub>O-CO<sub>2</sub> solubility in rhyolitic melts. *J. Volcanol. Geotherm.*  
624 *Res.* 143, 219-235.

625 McIntosh, I.M., Llewellyn, E.W., Humphreys, M.C.S., Nichols, A.R.L., Burgisser, A., Schipper, C.I.,  
626 and Larsen, J.F., 2014. Distribution of dissolved water in magmatic glass records growth and  
627 resorption of bubbles. *Earth Planet. Sci. Lett.* 401, 1-11.

628 Newman, S., Epstein, S., and Stolper, E., 1988. Water, carbon dioxide and hydrogen isotopes in  
629 glasses from the ca. 1340 A.D. eruption of the Mono Craters, California: Constraints on  
630 degassing phenomena and initial volatile content. *J. Volcanol. Geotherm. Res.* 35, 75–96.

631 Okumura, S., Nakamura, M., Nakashima, S., 2003. Determination of molar absorptivity of IR  
632 fundamental OH stretching vibration in rhyolitic glasses. *Am. Mineral.* 88, 1657-1662.

633 Okumura, S., Nakamura, M., Takeuchi, S., Tsuchiyama, A., Nakano, T., and Uesugi, K., 2009.  
634 Magma deformation may induce non-explosive volcanism via degassing through bubble  
635 networks. *Earth Planet. Sci. Lett.* 281(3-4) 267-274.

636 Pitzer, K.S., and Sterner, S.M., 1994. Equations of state valid continuously from zero to extreme  
637 pressures for H<sub>2</sub>O and CO<sub>2</sub>. *J. Chem. Phys.* 101, 311.

638 Rust, A.C., and Cashman, K.V., 2007. Multiple origins of obsidian pyroclasts and implications for  
639 changes in the dynamics of the 1300 B.P. eruption of Newberry Volcano, USA. *Bull. Volcanol.*  
640 69, 825–845.

641 Rust, A.C., Cashman, K.V., and Wallace, P.J., 2004. Magma degassing buffered by vapor flow  
642 through brecciated conduit margins. *Geology* 32, 349–352.

643 Taylor, B.E., 1991. Degassing of Obsidian Dome rhyolite, Inyo volcanic chain, California. *Geochem.*  
644 *Soc. Spec. Pub.* 3, 339-353.

645 Taylor, B.E., Eichelberger, J.C., and Westrich, H.R., 1983. Hydrogen isotopic evidence of rhyolitic  
646 magma degassing during shallow intrusion and eruption. *Nature* 306, 541–545.

647 Tuffen, H., Dingwell, D. B., 2005, Fault textures in volcanic conduits: evidence for seismic trigger  
648 mechanisms during silicic eruptions, *Bulletin of Volcanology*, v. 67, no. 4, p. 370–387.

649 Tuffen, H., Dingwell, D.R., and Pinkerton, H. (2003) Repeated fracture and healing of silicic  
650 magma generate flow banding and earthquakes? *Geology*, 31, 1089-1092.

651 Vasseur, J. and Wadsworth, F.B., 2017. Sphere models for pore geometry and fluid permeability  
652 in heterogeneous magmas. *Bulletin of Volcanology*, 79(11), p.77

653 Wadsworth, F.B., Vasseur, J., von Aulock, F.W., Hess, K.U., Scheu, B., Lavallée, Y., and Dingwell,  
654 D.B., 2014. Nonisothermal viscous sintering of volcanic ash. *J. Geophys. Res.* 119, 8792–8804.

655 Wadsworth, F.B., Vasseur, J., Llewellyn, E.W., Schaubroth, J., Dobson, K.J., Scheu, B. and Dingwell,  
656 D.B., 2016. Sintering of viscous droplets under surface tension. *Proc. R. Soc. A*, 472(2188),  
657 p.20150780

658 Wadsworth, F.B., Vasseur, J., Llewellyn, E.W., Dobson, K.J., Colombier, M., von Aulock, F.W.,  
659 Fife, J.L., Wiesmaier, S., Hess, K.U., Scheu, B. and Lavallée, Y., 2017. Topological inversions in  
660 coalescing granular media control fluid-flow regimes. *Physical Review E*, 96(3), p.033113.  
661 Walker, G.P.L., 1981. Plinian eruptions and their products. *Bull. Volcanol.* 44, 223-240.  
662 Watkins, J.M., Gardner, J.E., and Befus, K.S., 2017. Non-equilibrium degassing, regassing, and  
663 vapor fluxing in magmatic feeder systems. *Geology* 45, 183-186.  
664 Zhang, Y., and Ni, H., 2010. Diffusion of H, C, and O components in silicate melts. *Rev. Mineral.*  
665 *Geochem.* 72, 171-225.  
666 Zhang, Y., Belcher, R., Ihinger, P.D., Wang, L., Xu, Z., and Newman, S., 1997. New calibration of  
667 infrared measurement of dissolved water in rhyolitic glasses. *Geochim. Cosmochim. Acta*  
668 61, 3089-3100.  
669  
670

671 **Figure Captions:**

672

673 **Figure 1:** Sample porosity ( $\phi$ , in vol.%) as a function of experimental sintering time. High and  
674 low porosities of heterogenous samples are linked by vertical tie lines. All porosities are  
675 precise to  $\pm 10\%$ . Experiments of coarse ash only ran for 30 and 60 minutes, but did not  
676 sinter. The equilibrium porosity of  $\phi = 3$  vol.% is shown as a dashed line (Wadsworth et al.,  
677 2016; Gardner et al., 2018).

678

679 **Figure 2:** Photomicrographs of sintered unimodal ash. (a) Binary threshold image of G-1766 (fine  
680 ash,  $t = 5$  minutes) with incipiently sintered particles (white) dispersed in a continuous porous  
681 network (black). (b) Reflected light image of G-1728 (fine ash,  $t = 20$  minutes) with dense glass  
682 and dispersed, contorted vesicles (in black). (c) Transmitted light image of the same sample  
683 in (b) with isolated spherical (arrows) and highly contorted vesicles. Dashed line traces one  
684 chain of connected vesicles. (d) Transmitted light image of G-1759 (fine ash,  $t = 47$  minutes)  
685 with isolated, contorted vesicles (arrows). (e) Transmitted light image of G-1758 (fine ash,  $t$   
686 = 60 minutes) with only spherical vesicles. (f) Reflected light image of G-1772 (wet ash,  $t = 30$   
687 minutes) with incipiently sintered particles dispersed in a continuous porous network, now  
688 mainly filled with epoxy.

689

690 **Figure 3:** Sintering textures of fine ash samples (open circles) as a function of equilibrium melt  
691 viscosity ( $\eta_e$ , in log Pa s) and experimental time. Solid lines demark approximate phases of  
692 constant texture. In Phase 1, individual particles remain loose and lack cohesion. In Phase 2,



693 particles are sintered only at their contacts and porosity is fully open. In Phase 3, particles  
694 are merged together and vesicles are nearly sealed, but many vesicles are still multi-cusped  
695 shaped. In Phase 4, samples are dense glass with isolated vesicles. Dashed curves (with small  
696 numbers) are for coarser ash sintered in Gardner et al. (2018).

697

698 **Figure 4:** Photomicrographs of sintered bimodal samples (all scale bars are 200  $\mu\text{m}$  long). (a)

699 Reflected light image of G-1724 (50:50 fine:coarse ash,  $t = 20$  minutes;) with incipiently

700 sintered particles in a continuous porous network, now mainly filled with epoxy. (b) Reflected

701 light image of G-1760 (50:50 fine:coarse ash,  $t = 45$  minutes) with highly porous matrix

702 between closely spaced large particles; dashed line traces a large continuous pocket of large

703 vesicles  $>1$  mm long. (c) Reflected light image of same sample as (b) but with low porosity

704 matrix where large particles are far apart. (d) Transmitted light image of G-1762 (50:50

705 fine:coarse ash,  $t = 60$  minutes) with homogeneous matrix with spherical vesicles (arrows)

706 between large relict particles. (e) Reflected light image of G-1763 (75:25 fine:coarse ash  $t =$

707 45 minutes) with homogeneous porous matrix amongst large particles (outlined in white).

708 Large vesicle in the middle is part of a longer pocket  $\sim 300$   $\mu\text{m}$  long. (f) Reflected light image

709 of G-1767 (50:50 fine:wet ash,  $t = 20$  minutes) with highly porous matrix between closely

710 spaced large particles; dashed lines trace continuous pockets of large vesicles.

711

712 **Figure 5.** Temperature versus total run duration for fine ash samples that were either sintered at

713 750°C (open circles) or sintered at 750°C and then cooled (solid circles). Final porosity (vol.%)

714 values are listed next to each sample. Note that samples plot along nearly linear cooling lines  
715 (solid curves), showing that cooling occurred at a relatively steady rate.

716

717 **Figure 6:** (a) Reflected and (b) transmitted light images of G-1729 that sintered for 30 minutes at  
718 750°C and then quenched. (c) Reflected and (d) transmitted light images of G-1789 that  
719 sintered for 10 minutes at 750°C and then cooled to 550°C, over 25 minutes. Both have ~3  
720 vol.% vesicles, but all are distorted in G-1789 (some marked by arrows), whereas half are  
721 spherical in G-1729. Images (a) and (c) are 400  $\mu\text{m}$  x 400  $\mu\text{m}$ ; scale bars in (b) and (d) are 50  
722  $\mu\text{m}$  long.

723

724 **Figure 7:** Porosity ( $\phi$ , vol.%) as a function of sintering time for samples that started with dry  
725 ash; symbols are the same as in Figure 1; porosities are precise to  $\pm 10\%$ . Curves for  
726 solutions of equation 3 for low- $P_c$  sintering are shown for unimodal fine ash (solid lines) and  
727 unimodal coarse ash (dashed lines), assuming  $\phi_i = 45$  or 60 vol.%. All mixed fine-coarse  
728 bimodal samples fall between the end-member cases. The equilibrium porosity of  $\phi =$   
729 3 vol.% is given as a limiting value (Wadsworth et al., 2016; Gardner et al., 2018).

730

731 **Figure 8:** Estimated duration of cooling step (over interval 750-550°C) required to resorb bubbles  
732 of different initial size. Calculations (Appendix A) are based on simple scaling arguments and  
733 are indicative only. Solid black line is the cooling time required to diffusively resorb all H<sub>2</sub>O  
734 within a bubble; dashed black line is the characteristic timescale of viscous shrinkage of the  
735 bubble. Solid red line is the cooling time to 550°C for experimental run G-1783; solid blue line

736 is the cooling time to 550°C for experimental run G-1729 (during rapid quench); grey box  
737 indicates range of initial bubble sizes expected in that sample. See main text for details.

738

739 **Figure 9:** Representative photomicrographs of North Mono obsidian pyroclasts (scale bars  
740 shown). (a) Transmitted light image of sample P4B-I with coexisting spherical (S) and  
741 distorted (D) vesicles. (b) Transmitted light image of sample P2-F with uniform distribution  
742 of spherical vesicles. (c) Transmitted light image of sample P10-E with bands of highly  
743 distorted vesicles. (d) Binary image of slice from High Resolution X-Ray Computed  
744 Tomography (HRXCT) scan of P10-E (same as in c) showing that vesicles (some marked by  
745 arrows) make up  $0.04 \pm 0.004$  vol.% of the obsidian. Widest length of sample is ~3 mm; see  
746 supplemental materials from Gardner et al. (2017) for scanning methods. (e) Transmitted  
747 light image of sample P4B-C with large pockets of vesicles dispersed in relatively dense glass  
748 with few vesicles. (f) Transmitted light image of sample P10-I that consists of bands of glass  
749 with numerous distorted vesicles (within the dashed lines) and regions of dense glass with  
750 very few vesicles. Watkins et al. (2017) found that vesicle-poor regions in P10-I tend to be  
751 rich in H<sub>2</sub>O, whereas the bands with abundant vesicles are rich in CO<sub>2</sub>.

752

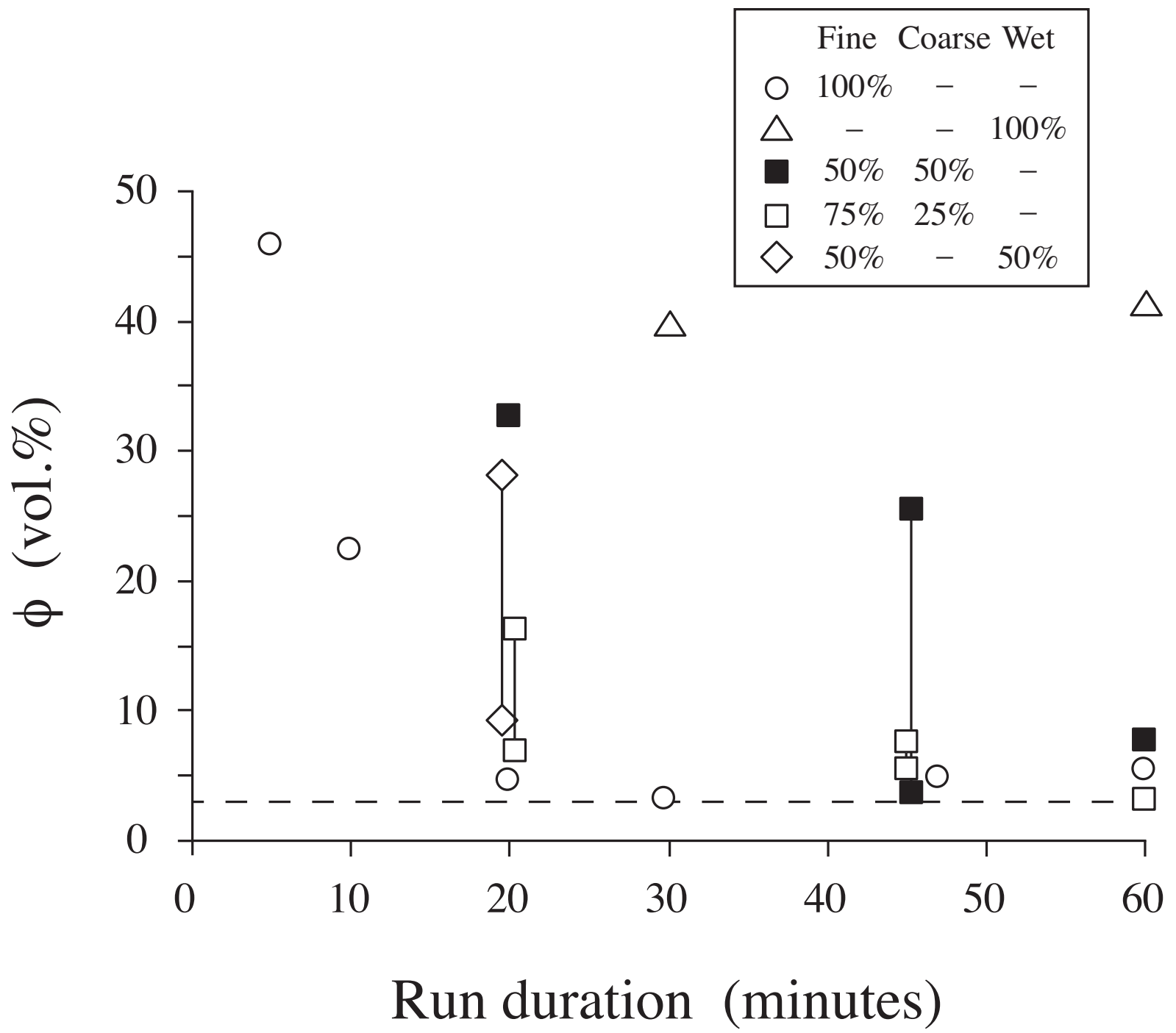


Figure 1

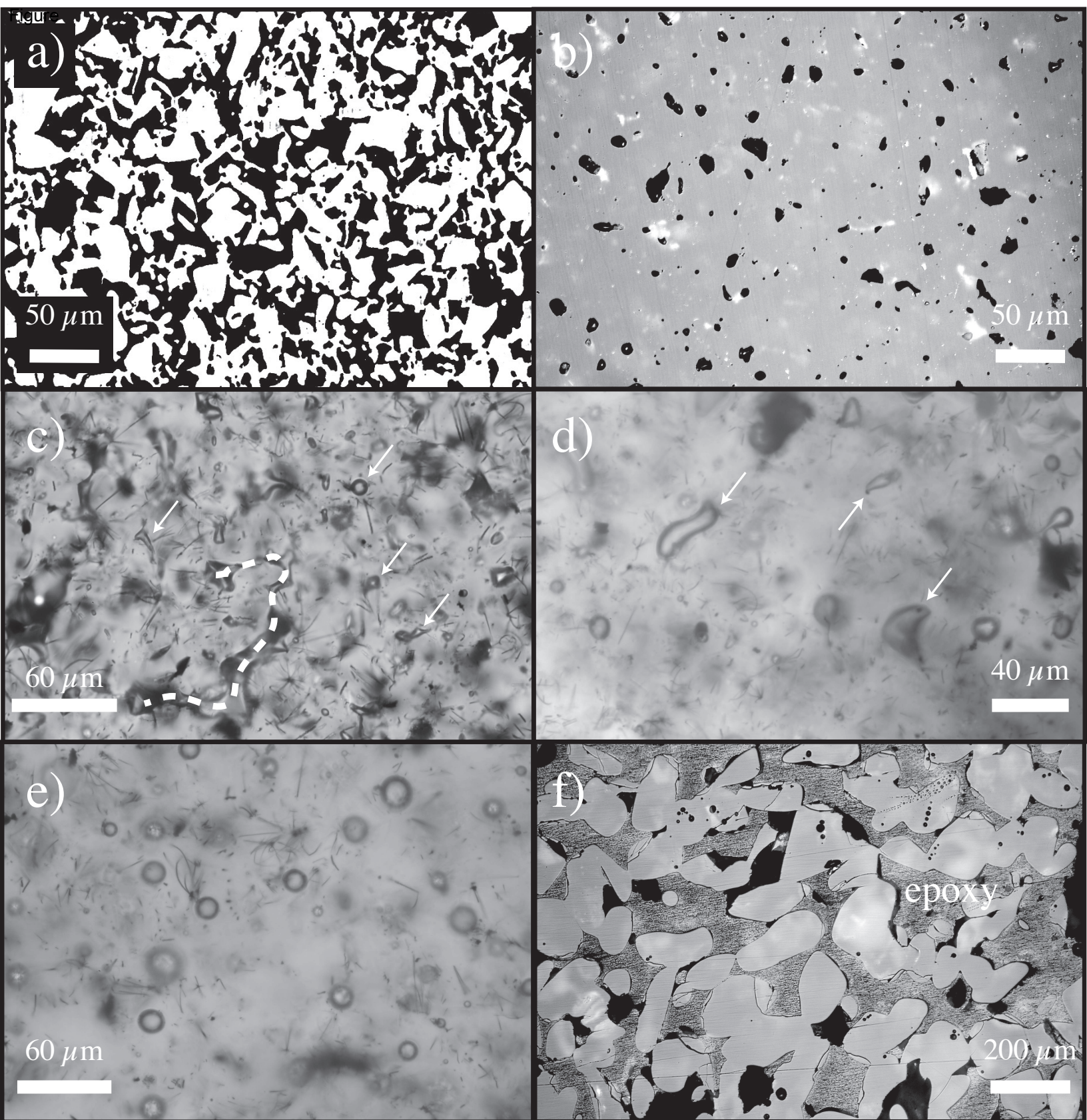


Figure 2

Figure

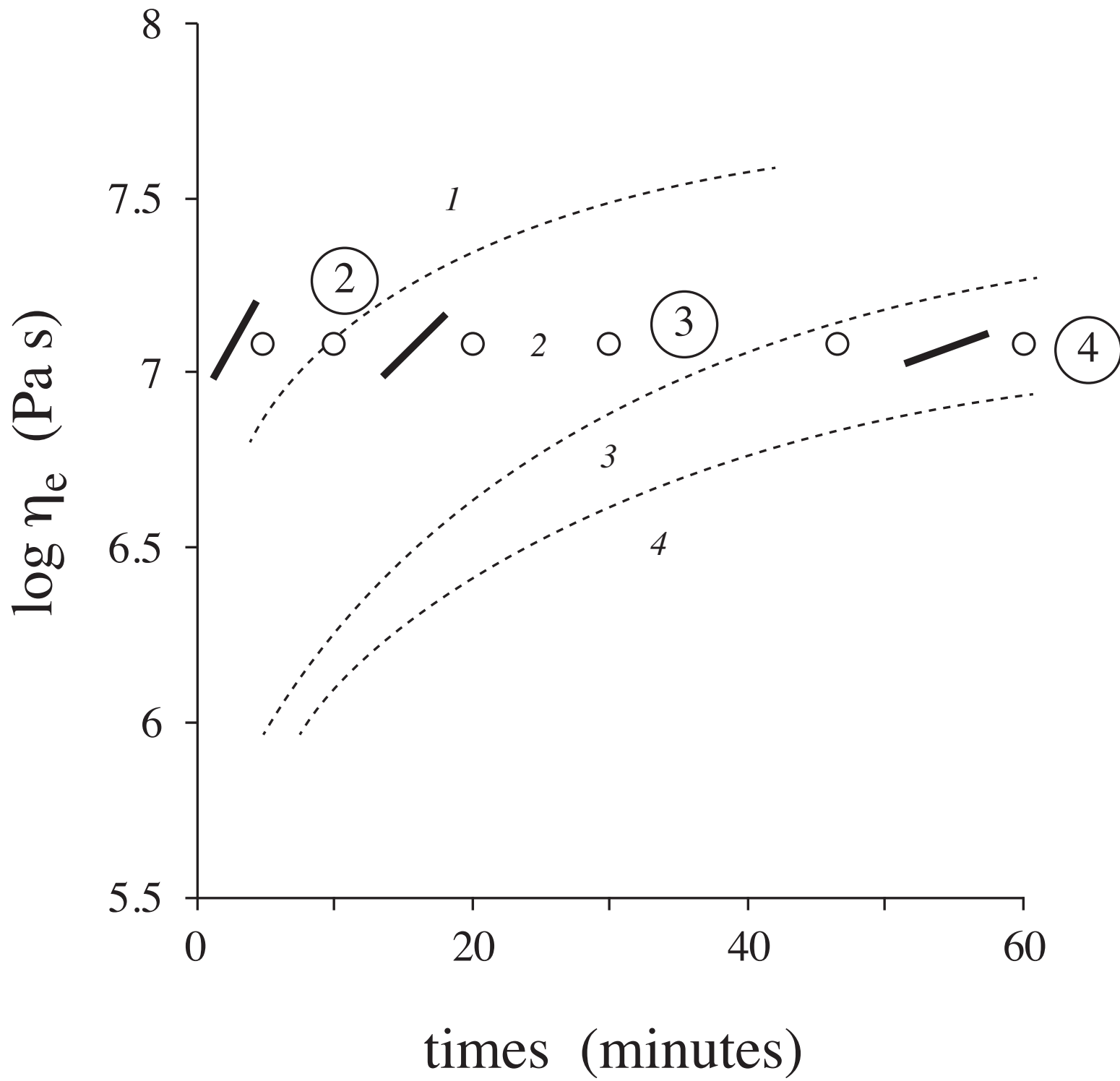


Figure 3



Figure

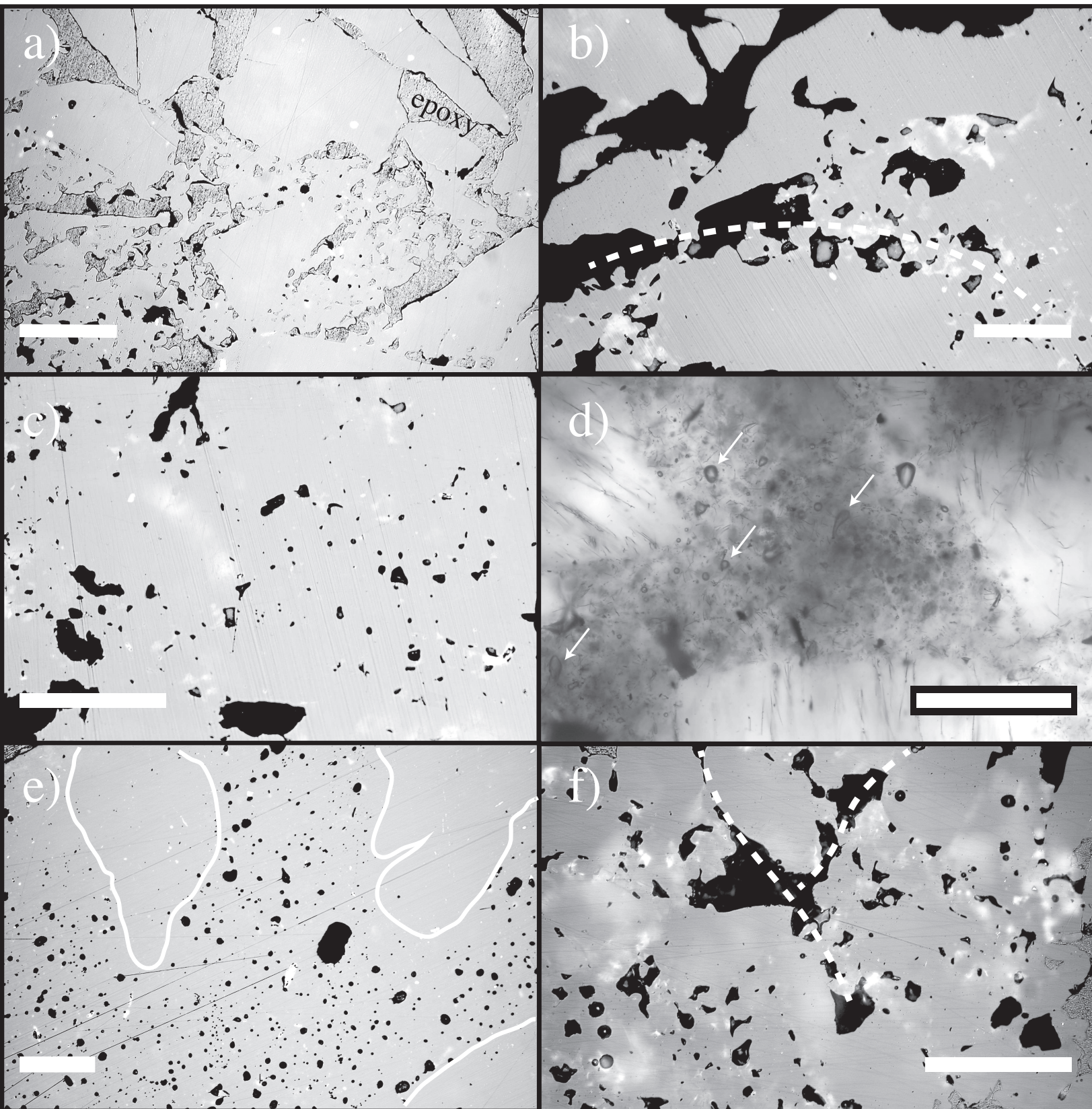


Figure 4

Figure

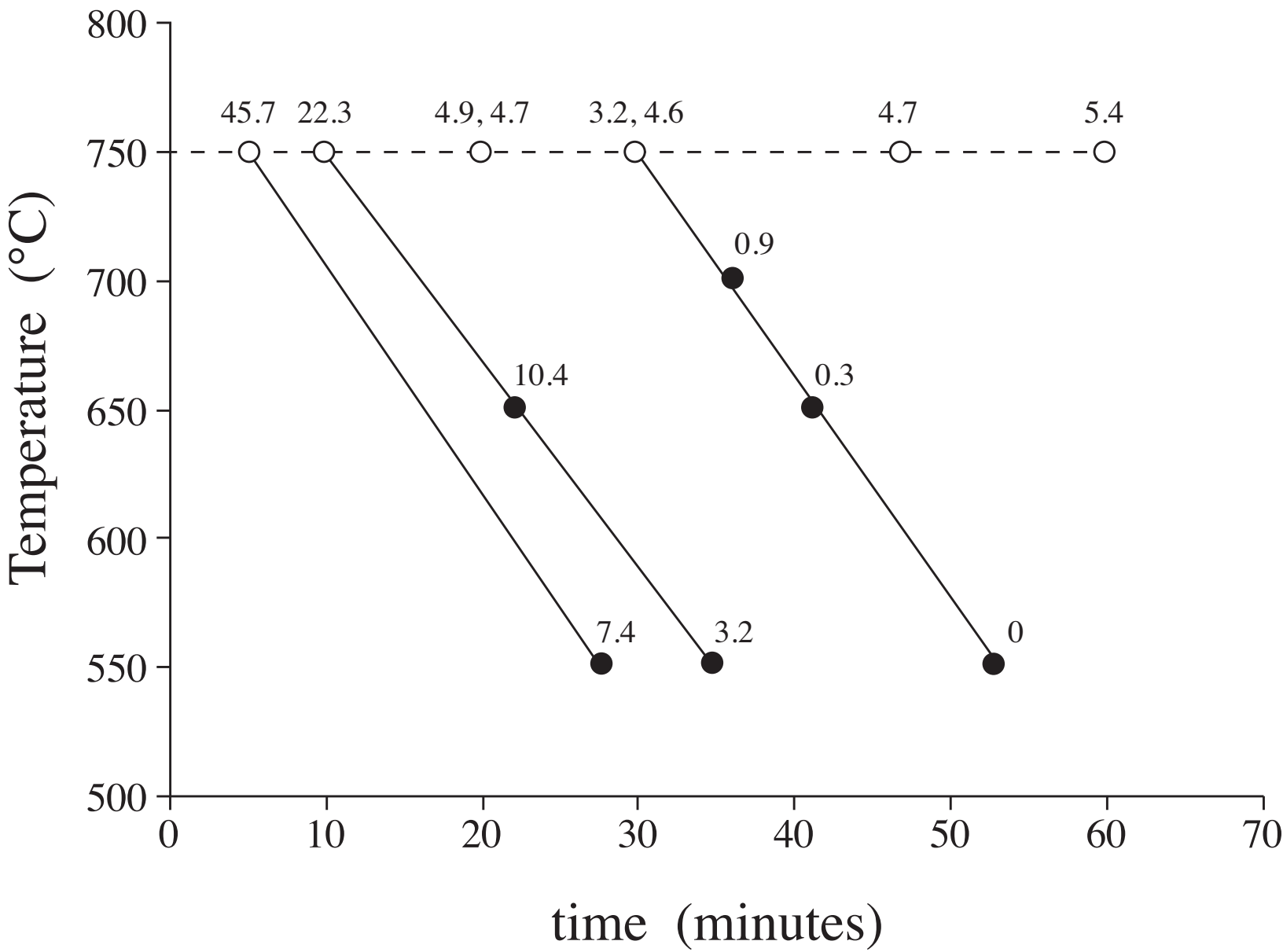


Figure 5



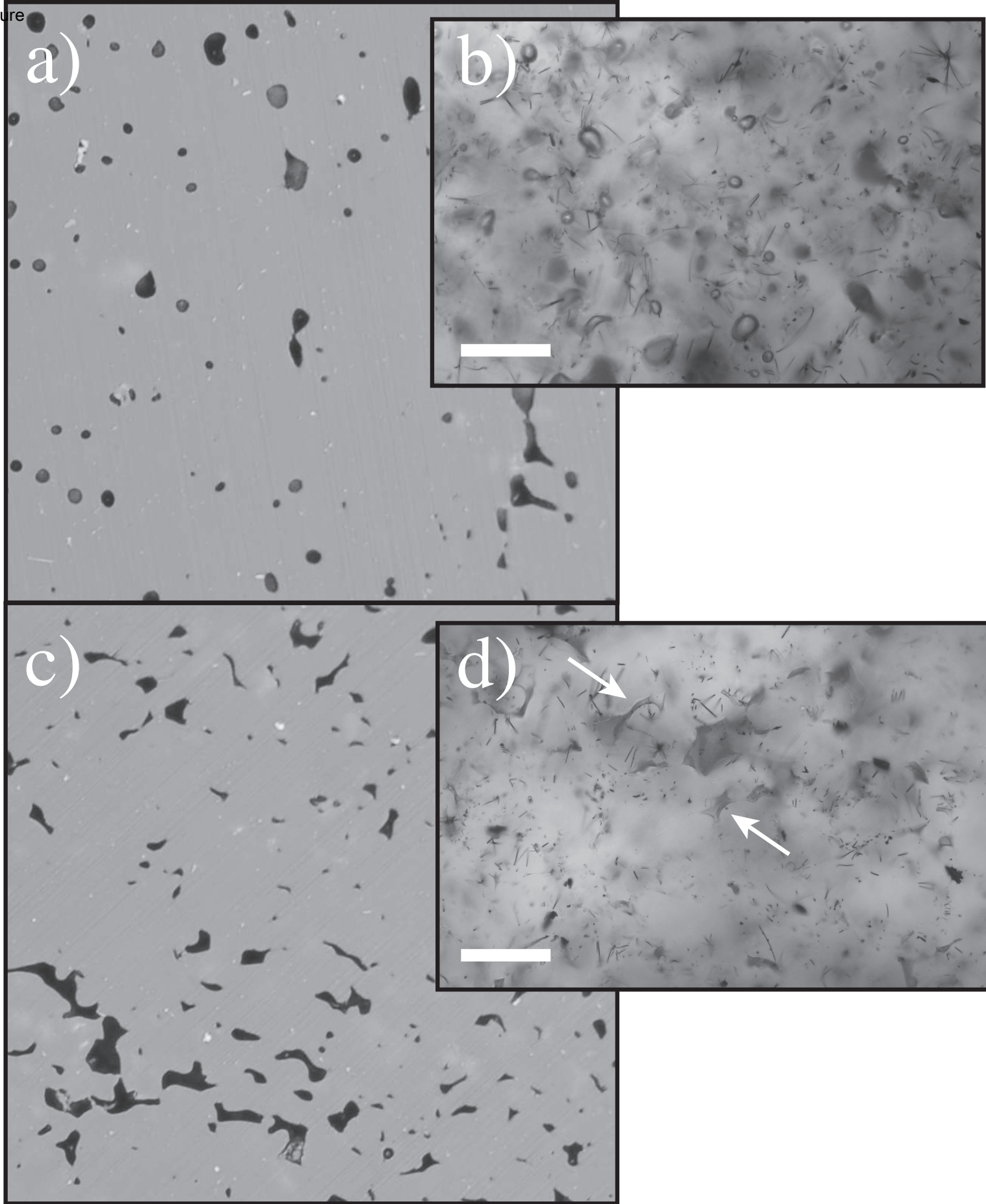


Figure 6

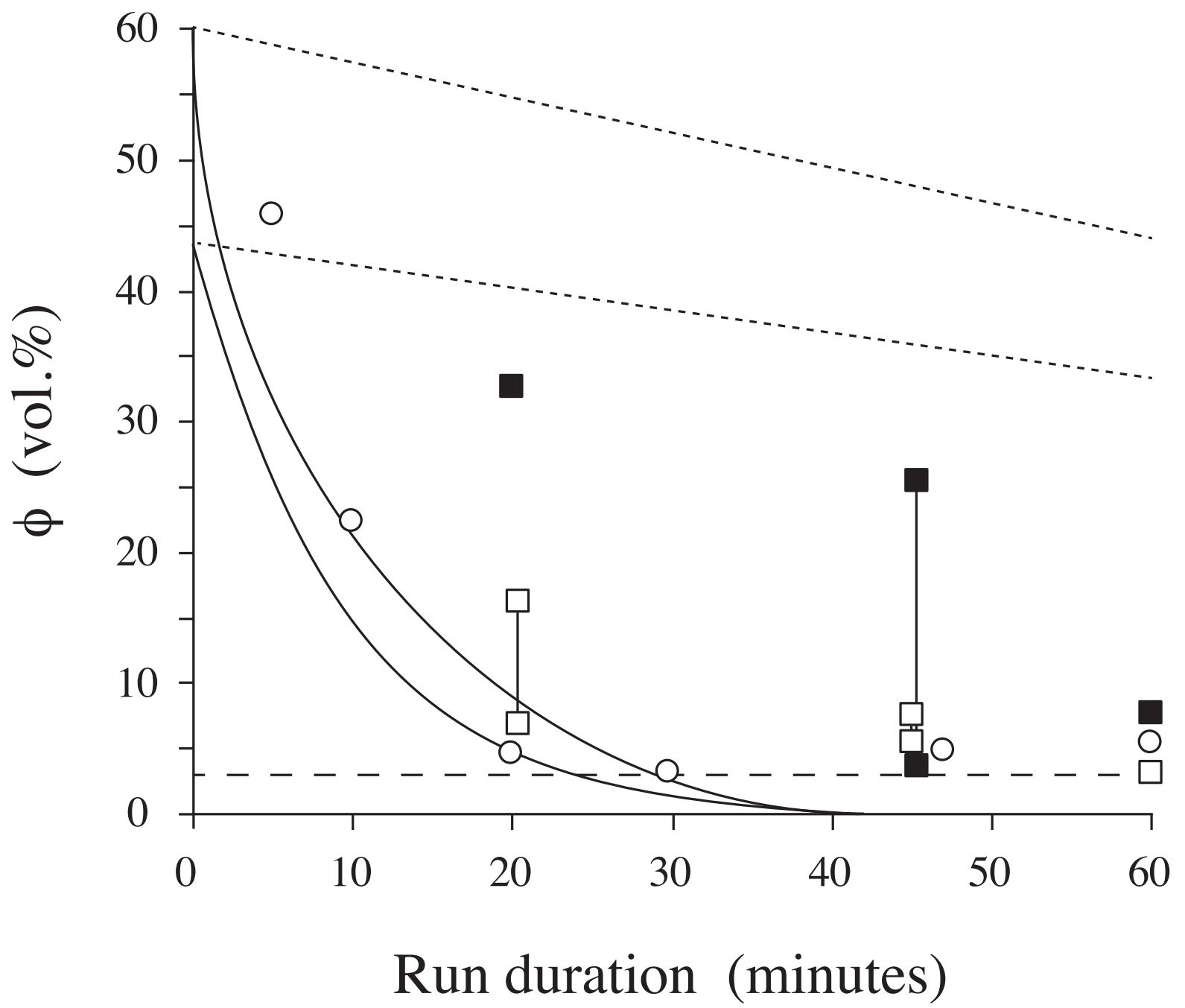
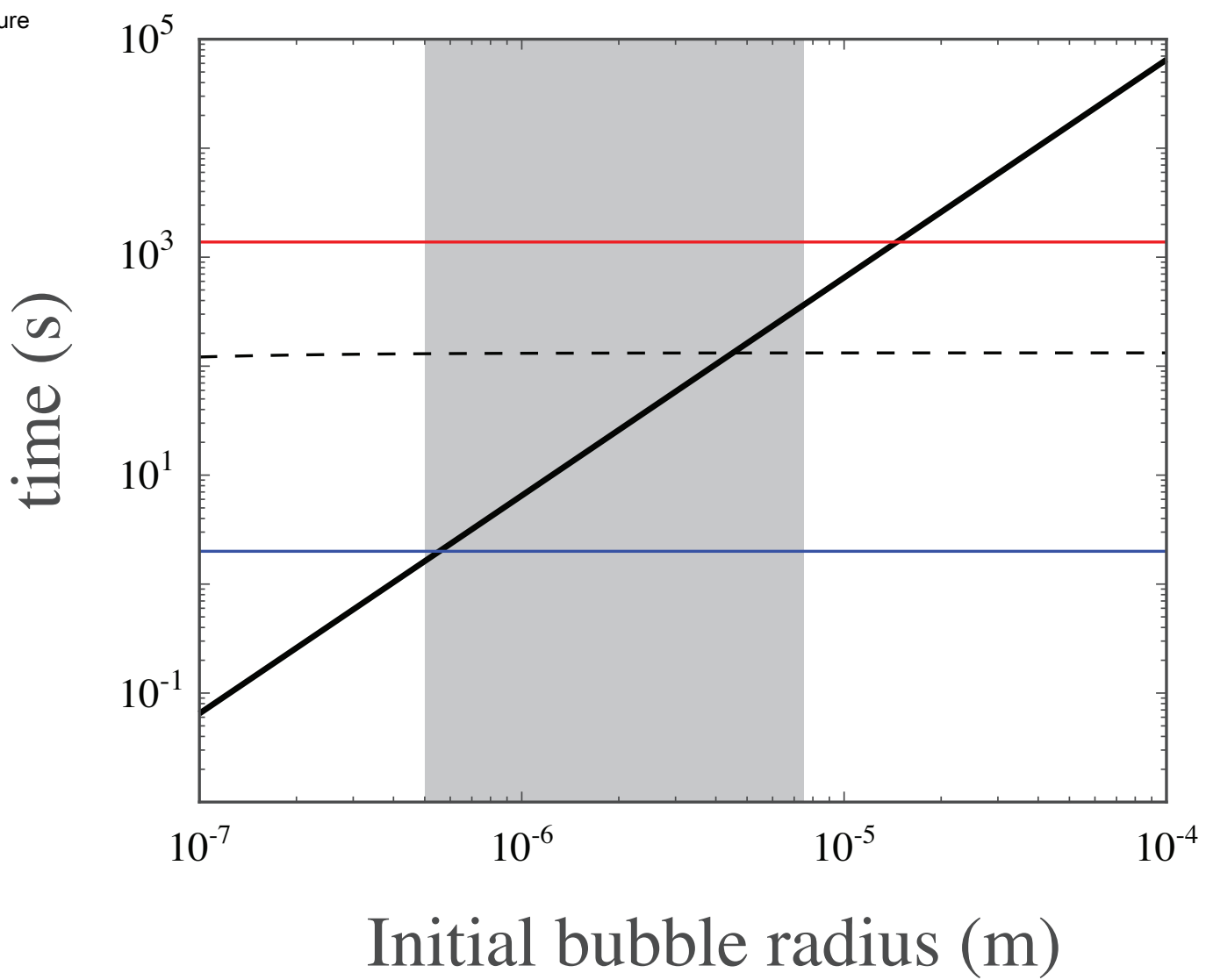


Figure 7



Figure

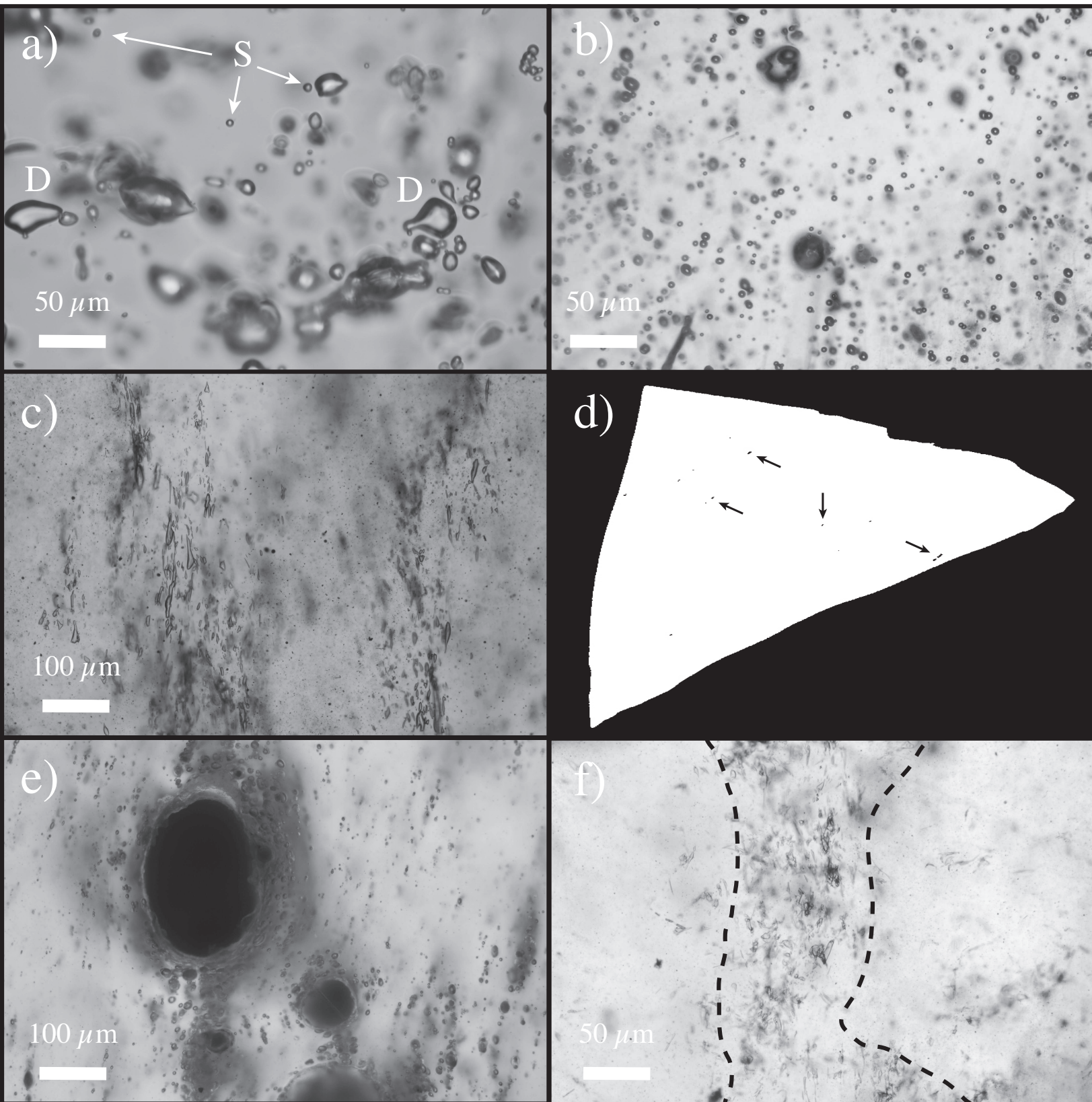


Figure 9

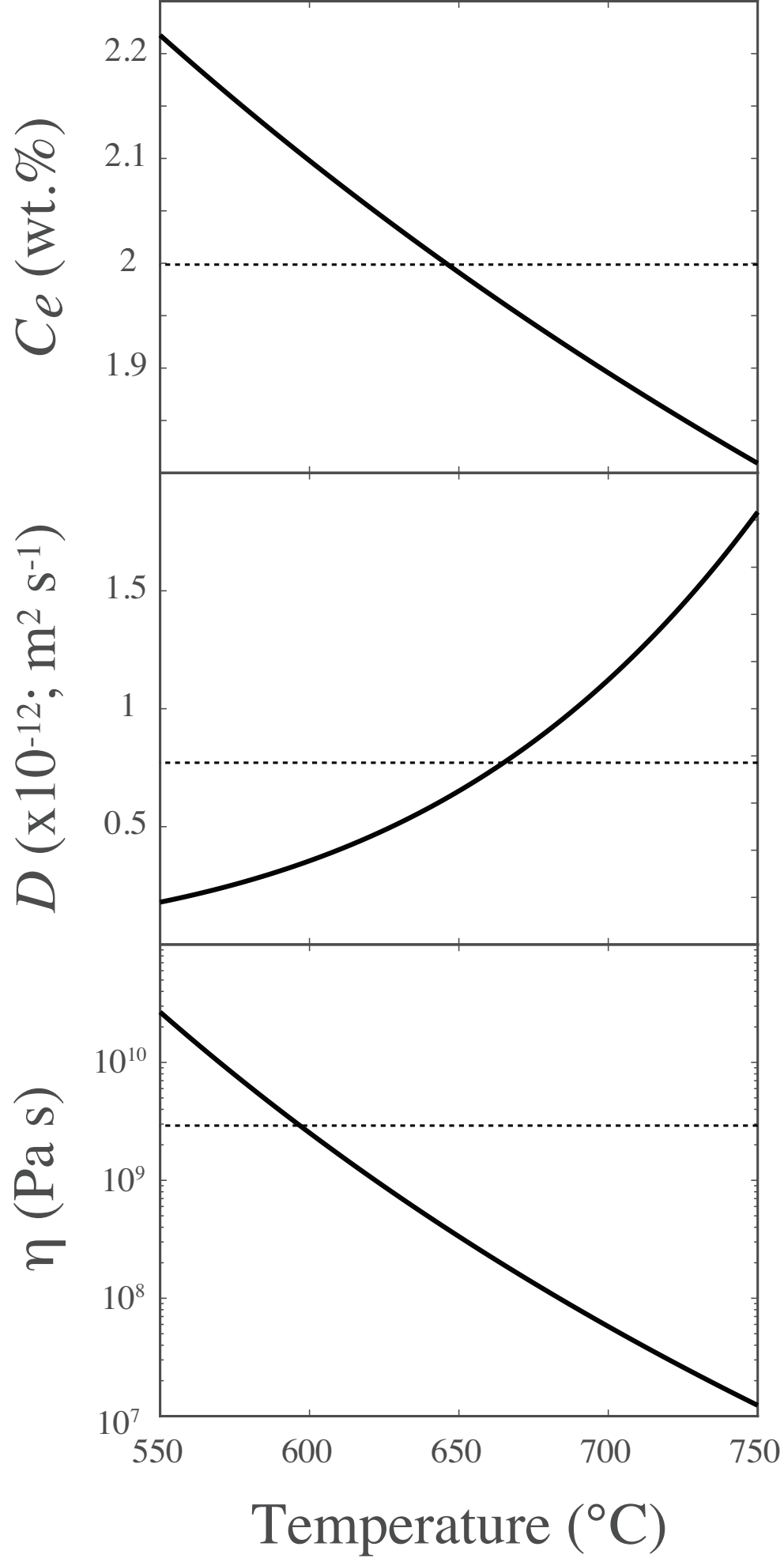


Figure A-1

**Table 1: Experimental Run Conditions and Results**

<i>Run</i> <sup>a</sup>	<i>P</i> <sup>b</sup> (MPa)	<i>T</i> <sup>b</sup> (°C)	<i>t</i> <sup>b</sup> (min)	Fine <sup>c</sup> (mg)	Coarse <sup>c</sup> (mg)	Wet <sup>c</sup> (mg)	$\phi$ <sup>d</sup> (vol.%)	$\log N_v^e$ (cm <sup>-3</sup> )	Size <sup>e</sup> ( $\mu$ m)
G-1766	22	750	5	31.3	0	0	45.7	n.d.	–
G-1765	22	750	10	30.1	0	0	22.3	n.d.	–
G-1728	22	750	20	31.4	0	0	4.9	7.80	2–4
G-1729	22	750	30	31.9	0	0	3.2	7.66	1–15
G-1759	22	750	47	32.2	0	0	4.7	7.53	1–38
G-1758	22	750	60	32.8	0	0	5.4	7.50	2–48
G-1769	22	750	30	0	42.1	0	n.d.	n.d.	–
G-1768	22	750	60	0	40.2	0	n.d.	n.d.	–
G-1772	22	750	30	0	0	39.7	34.6	n.d.	–
G-1773	22	750	60	0	0	41.2	31.9	n.d.	–
G-1724	22	750	20	20.2	20.5	0	32.6	n.d.	–
G-1760	22	750	45	20.4	22.0	0	25.5/3.5	7.20	n.d.
G-1762	22	750	60	19.7	20.9	0	7.6	7.34	1–20
G-1761	22	750	20	30.0	10.0	0	16.2/6.7	7.54	1–10
G-1763	22	750	45	30.6	9.3	0	7.4/5.4	7.63	1–16
G-1764	22	750	60	30.0	10.2	0	3.1	7.59	1–84
G-1767	22	750	20	15.1	0	15.5	27.9/9.0	7.75	1–20

(a) Composition of obsidian used in all experiments (all oxides in wt.%, with all Fe reported as FeO: SiO<sub>2</sub> = 76.53; TiO<sub>2</sub> = 0.06; Al<sub>2</sub>O<sub>3</sub> = 13.01; FeO\* = 0.79; MnO = 0.08; MgO = 0.02; CaO = 0.74; Na<sub>2</sub>O = 3.87; K<sub>2</sub>O = 4.91.

(b) Pressure (in MPa), temperature (in °C), and run duration (in minutes) of the experiment.

(c) Mass of “fine” (dry,  $\leq 45 \mu$ m), “coarse” (dry, 250–500  $\mu$ m) and wet (hydrated, 125–180  $\mu$ m) powders in sample.

(d) Porosity (in vol.%) of the experiment, including all vesicle types. If two values are listed, the first is porosity of matrix between closely spaced large particles, and the second is the porosity of the matrix far away from large particles.

(e) Number density (in numbers per cubic centimeter) of all vesicles present and range of sizes of spherical vesicles only; n.d. = not determined; – means no spherical vesicles present.



**Table 2: Cooling Experiments, Conditions and Results**

Run	$P^a$ (MPa)	$T_s^a$ (°C)	$t_s^a$ (min)	$T_f^b$ (°C)	$t_f^b$ (min)	Fine <sup>c</sup> (mg)	Coarse <sup>c</sup> (mg)	$\phi^d$ (vol.%)	$\log N_v^e$ (cm <sup>-3</sup> )	Size <sup>e</sup> ( $\mu\text{m}$ )
G-1788	22	750	5	550	22:44.6	30.7	0	7.4	n.d.	n.d.
G-1787	22	750	10	650	12:06.6	32.3	0	10.4	n.d.	n.d.
G-1789	22	750	10	550	24:53.4	34.3	0	3.2	n.d.	n.d.
G-1786	22	750	30	700	6:10.2	29.4	0	0.9	6.83	n.d.
G-1784	22	750	30	650	11:17.3	30.3	0	0.3	5.41	15–35
G-1783	22	750	30	550	22:56.7	30.3	0	0	0*	0
G-1785	22	750	30	650	11:01.2	20.2	20.8	15.9/1.8	6.25	n.d.

(a) Pressure (in MPa) and temperature (in °C) of sintering for duration  $t$  (in minutes).

(b) Final temperature (in °C) of cooling and duration of cooling (in minutes) to final temperature.

(c) Mass of “fine” (dry,  $\leq 45 \mu\text{m}$ ) and “coarse” (dry, 250–500  $\mu\text{m}$ ) powders in sample.

(d) Porosity (in vol.%) of the experiment, including all vesicle types. If two values are listed, the first is the porosity of matrix between closely spaced large particles, and the second is porosity of matrix far away from coarse particles.

(e) Number density (in numbers per cubic centimeter) and range of sizes of all vesicles present; n.d. = not determined.  $N_v$  in G-1783 is 0 per cm<sup>3</sup>.